applied sciences

MDPI

Article

Experimental and Analytical Study of an Anode-Supported Solid Oxide Fuel Cell

Shadi Salehian [1], Joy Marie Mora [1], Haoyu Li [1], Daniel Esau [2], Min Hwan Lee [1], André Weber [2] and Po-Ya Abel Chuang [1,*]

[1] Department of Mechanical and Aerospace Engineering, University of California, Merced, CA 95343, USA; ssalehian2@ucmerced.edu (S.S.); jmora105@ucmerced.edu (J.M.M.); hli84@ucmerced.edu (H.L.); mlee49@ucmerced.edu (M.H.L.)

[2] Institute for Applied Materials—Electrochemical Technologies (IAM-ET), Karlsruhe Institute of Technology (KIT), D-76131 Karlsruhe, Germany; andre.weber@kit.edu (A.W.)

* Correspondence: abel.chuang@ucmerced.edu

Abstract

A zero-dimensional, non-isothermal analytical framework was developed to assess solid oxide fuel cell (SOFC) performance across a broad range of operating conditions. The model integrates the anode, electrolyte, interlayers, and cathode, while resolving the distinct physicochemical processes within each layer. Electrochemical impedance spectroscopy (EIS), followed by distribution of relaxation times (DRT) analysis, was implemented to probe relevant cell polarization resistances under open-circuit and load conditions. The modeling framework couples mass and charge transport, electrochemical reactions, and non-isothermal heat transfer, with multilayer discretization applied to capture localized material properties and operating conditions. It enables the estimation of electrolyte ionic conductivity and total ohmic resistance by accounting for microstructural and geometric parameters, while also quantifying activation energies, exchange current densities, and gas-diffusion-related polarization resistances. Simulations were conducted for an SOFC operating on pure hydrogen with varying oxygen concentrations at 700 °C, 660 °C, 620 °C, and 580 °C. The results were validated against experimental data. The analysis revealed that ohmic overpotential dominates total cell losses, even at high current densities, underscoring the importance of minimizing ionic resistance to improve overall SOFC performance.

Keywords: solid oxide fuel cell; electrochemical impedance spectroscopy (EIS); polarization losses; distribution of relaxation times (DRT); modeling

Check for updates

Academic Editors: Zhihua Deng, Lixin Fan, Magdalena Dudek and Shengqiu Zhao

Received: 1 January 2026
Revised: 20 January 2026
Accepted: 29 January 2026
Published: 2 February 2026

1. Introduction

Solid oxide fuel cells (SOFCs) have garnered considerable attention for their ability to achieve high efficiencies while operating without expensive precious-metal catalysts [1,2]. These devices enable the direct utilization of a wide range of fuels, including hydrogen, syngas, and heavier hydrocarbons [3], owing to their high operating temperatures (typically 600–1000 °C) [4,5]. The use of yttria-stabilized zirconia (YSZ) as a solid electrolyte provides a robust oxygen-ion-conducting medium that is critical for maintaining high ionic conductivity [6]. In addition to their high conversion efficiency [7,8], SOFCs offer environmental benefits due to low emissions and fuel flexibility without the extensive need for reforming [9,10]. Despite these advantages, challenges remain that impact the long-term reliability and performance prediction of SOFC systems, including degradation mechanisms such as anode coking [11], gas poisoning [12,13], nickel migration in Ni–YSZ anodes [14–16], and thermal expansion mismatch

https://doi.org/10.3390/app16031497

between ceramic components [17–19]. The high operating temperatures (typically above 700 °C) required by YSZ-based electrolytes further lead to increased costs, slow thermal cycling, performance degradation, and system complexity [4,20,21]. These issues complicate the accurate modeling of different transport mechanisms and processes, which are critical for optimizing SOFCs' performance and durability.

Extensive experimental research has focused on improving the performance and longevity of SOFCs by optimizing key component materials, particularly Ni-YSZ cermet anodes and LSCF-based cathodes, which play critical roles in electrochemical activity and thermal compatibility [22]. Beyond conventional Ni–YSZ and LSCF architectures, exsolution-based perovskite electrodes have demonstrated enhanced durability by forming multimetallic nanoparticles with dopant-dependent exsolution kinetics that enhance catalytic stability [23]. Studies have also systematically explored the effects of varying operating conditions, including fuel and oxidant compositions, humidity levels, and operating temperatures, to mitigate degradation and maximize efficiency [24]. While these experimental efforts have provided valuable insights into electrochemical kinetics, mass transport behavior, and degradation mechanisms, they are often limited by high costs, extensive testing durations, and the inherent difficulty of isolating individual loss processes. To overcome these limitations, modeling has become an essential complementary approach for SOFC research, enabling the rapid exploration of parameter effects and decoupling overlapping loss mechanisms.

Considerable modeling efforts have been devoted to understanding electrochemical and transport phenomena in SOFCs. Numerical and computational methods, such as finite element modeling (FEM) and computational fluid dynamics (CFD), have been widely employed to simulate the coupled effects of mass, charge, and heat transport within the cell architecture [25,26]. The three-dimensional models developed by Wang et al. [27], Yakabe and Sakurai [28], and Gubner [29,30] have provided detailed spatial predictions of SOFC behavior under various operating conditions.

While numerical models offer detailed insights, they are computationally intensive and often require extensive material-property datasets. To address this, analytical models have been developed based on simplifying assumptions that retain key physics while allowing for closed-form solutions. One-dimensional analytical models along the electrode thickness have been proposed by Aloui et al. [31], Bao et al. [32], Zhao et al. [33], and Hussain et al. [34], enabling the separation and quantification of activation, diffusion, and ohmic losses. Microstructurally resolved models, such as those by Costamagna et al. [35] and Chan and Xia [36], emphasize the role of finite reaction zones and electrode morphology in performance. Pramuanjaroenkij et al. [37] further demonstrated the influence of electrolyte material and operating temperature, while Grimes et al. [38] highlighted the potential of microstructural modifications to enhance durability. Compact 0-D and isothermal models have also been used effectively for system-level predictions. Leonide et al. [39] proposed a zero-dimensional isothermal model for fuel-electrode-supported SOFCs and demonstrated its validity through experimental comparison. Compared with numerical approaches, analytical models offer substantial advantages for early-stage design, rapid parametric studies, and independent diagnosis of dominant polarization losses. Their lower computational demand and their ability to separately model activation, ohmic, and diffusion losses make them especially suitable for understanding SOFCs' performance under varying temperatures and gas compositions, as demonstrated in this study.

Electrochemical impedance spectroscopy (EIS) combined with distribution of relaxation times (DRT) analysis has become a powerful approach for analyzing the complex polarization processes in SOFCs. By mathematically deconvoluting the impedance spectrum, DRT separates overlapping electrochemical phenomena with high resolution, allowing direct identification of individual polarization mechanisms [40]. This method has been applied to attribute distinct frequency peaks to physical processes, such as gas diffusion through porous anodes or charge transfer at electrode–electrolyte interfaces. For instance, Leonide et al. [39] resolved multiple electrode-specific processes using combined DRT and equivalent-circuit analysis. A low-frequency peak below approximately 1–10 Hz was attributed to gas-phase diffusion in the porous electrodes, while a mid-frequency feature in the ∼10–100 Hz range was associated with cathode activation polarization governed by oxygen surface exchange and bulk oxygen-ion transport in LSCF. At higher mid-frequencies ($\sim10^2$–10^3 Hz), an additional contribution was linked to anode gas diffusion within the anode functional layer, whereas high-frequency features ($\sim10^3$–10^4 Hz) were assigned to anode activation (charge transfer) polarization. Primdahl and Mogensen [24] used EIS and microstructural modeling to link anode gas diffusion behavior to porosity and tortuosity, findings later confirmed through DRT-based parameter extraction. Furthermore, DRT has been used to monitor degradation mechanisms in SOCs. Riegraf et al. [41] demonstrated that the evolution of specific DRT peaks over time could pinpoint dominant aging processes. Notably, DRT analysis improves SOFC modeling by extracting physically meaningful parameters that can be directly incorporated into equivalent-circuit or distributed models [42]. This integration enables the accurate decomposition of multistep electrode processes and strengthens model validation against experimental data across varying operating conditions.

In this work, a 0-D non-isothermal analytical model is developed to predict the performance of an anode-supported SOFC employing a Ni-YSZ fuel electrode and a composite LSCF-based air electrode. The model calculates activation, diffusion, and ohmic losses by incorporating kinetic and transport parameters extracted from EIS and DRT analyses under varying operating temperatures and inlet gas compositions. The model also incorporates a non-ideal ohmic loss term, accounting for interfacial and contact resistances that become significant at low operating temperatures and high current densities, thereby improving the accuracy of predicted cell performance. The residual difference between the total interfacial resistance and the measured ohmic resistance is treated as an effective interfacial term due to non-idealities and used for empirical fitting. In line with the impedance-based modeling framework established by Leonide et al. [43] and further implemented in subsequent works [44–46], this approach provides a physically grounded decomposition of performance losses based on experimentally derived parameters and combined EIS–DRT analyses, rather than relying solely on empirical polarization-curve-fitting. Model validation is conducted by comparing the model predictions with measured cell performance across multiple temperatures (700 °C, 660 °C, 620 °C, and 580 °C) and oxygen concentrations (100%, 50%, 20%, and 10% O_2). Key parameters, including ohmic resistances, activation energies, and diffusion coefficients, are extracted through regression of impedance spectra rather than empirical fitting, ensuring a rigorous, physics-based description of the system.

2. Materials and Methods

2.1. Experimental Cell Preparation and Assembly

All measurements were conducted on anode-supported solid oxide cells fabricated from commercially available half-cells (Kceracell, Boksu-myeon, Republic of Korea), which were sectioned into square specimens with dimensions of 2 cm × 2 cm. The resulting electrochemically active area was 0.1781 cm^2. Each cell comprised a multilayer architecture consisting of a 600 μm coarse composite NiO–YSZ support, a finer 26 μm NiO–YSZ anode functional layer, and a dense 5 μm yttria-stabilized zirconia (YSZ) electrolyte. On the air electrode, a dual-layer cathode configuration was employed. A mixed ionic–electronic conducting composite layer composed of $(La_{0.6}Sr_{0.4})_{0.95}Co_{0.2}Fe_{0.8}O_{3-\sigma}$ and $(Gd_{0.2}Ce_{0.8})O_{3-\sigma}$ (LSCF–GDC, 40 µm) served as the functional layer, while a pure LSCF layer (37 µm) functioned as the current-collector layer. To mitigate chemical interaction between the YSZ electrolyte and the strontium-containing cathode, a thin gadolinium-doped ceria interlayer (5 µm, 20% Gd) was introduced at the electrolyte–cathode interface. This interlayer suppresses the formation of insulating zirconate phases such as $LaZrO_3$ and $SrZrO_3$, thereby improving long-term electrochemical stability [47,48]. The schematic of the cell and the SEM of the cross-sectional area are presented in Figure 1.

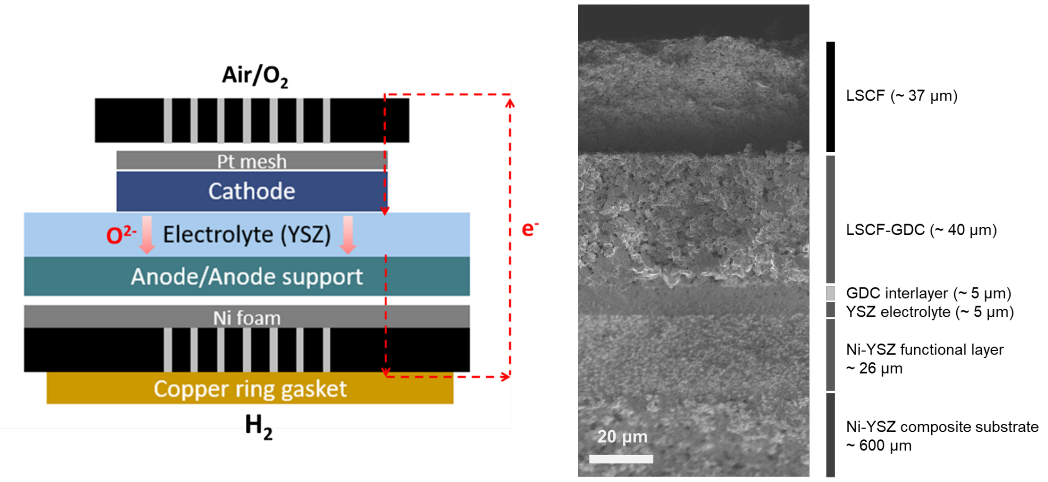

Figure 1. Schematic of the cell, and the cross-section's SEM showing each layer's thickness. Arrows indicate the directions of oxide-ion (O^{2-}) and electron (e^-) transport.

The GDC interlayer was fabricated using a screen-printing approach. The corresponding slurry was prepared by first dispersing a polymeric dispersant (Hypermer KD-1, Croda, Princeton, NJ, USA) in terpineol and stirring the mixture at 50 °C for 24 h. Subsequently, GDC nanopowder (20 mol% Gd, FuelCellMaterials, Lewis Center, OH, USA) and ethyl cellulose (Sigma-Aldrich, St. Louis, MO, USA) were incorporated, followed by an additional 24 h of stirring at the same temperature. The final composition of the slurry consisted of 40 wt% terpineol, 10 wt% Hypermer KD-1, 2 wt% ethyl cellulose, and 48 wt% GDC nanopowder. Slurries for the LSCF and LSCF–GDC cathode layers were prepared using an analogous procedure, with adjusted compositions , terpineol, 5 wt% Hypermer KD-1, 3 wt% ethyl cellulose, and 57 wt% of either LSCF or LSCF–GDC powder (FuelCellMaterials, Lewis Center, OH, USA). The GDC slurry was first screen-printed onto the YSZ electrolyte and subsequently sintered at 1150 °C for 5 h at a heating rate of 3 °C min^{-1}. Intermediate dwell steps at 80 °C (1 h) and 500 °C (30 min) were included to facilitate solvent evaporation and binder burnout. The LSCF–GDC layer was then printed atop the GDC interlayer and sintered at 1050 °C for 3 h under identical thermal conditions, followed by deposition and sintering of the LSCF current-collecting layer at 850 °C for 3 h. The LSCF–GDC nanocomposite functions as a graded transition layer that enhances interfacial connectivity relative to a single-phase LSCF cathode by increasing the density of electrochemically active sites and promoting efficient oxygen transport and charge transfer across the cathode–electrolyte interface [49,50]. The incorporation of the LSCF–GDC nanocomposite as a graded transition layer provides enhanced interfacial connectivity relative to a single-phase LSCF cathode. Electrical contact was established using a platinum mesh (Goodfellow, Pittsburgh, PA, USA) on the O_2/air electrode and a porous nickel foam on the fuel electrode. To ensure reliable mechanical and electrical contact between the electrodes and the current-collecting Pt mesh and Ni foam, a compressive load of 3 kg was applied uniformly across the cell assembly.

2.2. Physical and Electrochemical Characterizations

Microstructural characterization was carried out using field-emission scanning electron microscopy (FE-SEM, Zeiss Gemini 500, Zeiss, Oberkochen, Germany) operated at an accelerating voltage of 3 kV. FE-SEM was used to verify layer integrity and quantify the thickness of individual cell components. Prior to electrochemical testing, the cells were heated to 700 °C at a rate of 2.5 °C min^{-1} under a continuous flow of dry hydrogen at 100 sccm supplied to the fuel electrode. The reduction process was considered complete once the open-circuit voltage stabilized near 1.1 V, indicating full conversion of NiO to metallic Ni. Fuel cell performance was subsequently evaluated at operating temperatures of 580, 620, 660, and 700 °C. During these measurements, the oxygen electrode was supplied with O_2/N_2 mixtures containing 10–100% O_2 at a fixed total flow rate of 100 sccm, while the fuel electrode received 100 sccm of dry hydrogen. Following fuel cell operation, the same cells were tested under electrolysis conditions across the same temperature range. The influence of steam content on electrolysis performance was examined by controlling the relative humidity of the hydrogen feed gas. Steam was introduced by passing hydrogen through a temperature-regulated water bubbler to achieve relative humidities of 3%, 30%, and 50%. To avoid condensation, the entire fuel delivery line was maintained at elevated temperatures of 160 °C at the inlet and 170 °C at the outlet. On the air electrode, dry air was supplied (21% O_2 and 79% N_2) at a total flow rate of 100 sccm. Electrochemical measurements were performed using a Bio-Logic SP-200 potentiostat (BioLogic, Seyssinet-Pariset, France). Impedance spectra were collected under various applied overpotentials using a 10 mV AC perturbation over a frequency range spanning from 3 MHz to 200 mHz. Current–voltage characteristics were obtained via linear sweep voltammetry at a scan rate of 20 mV/s between 2.0 and 0.3 V. Distribution of relaxation times (DRT) analysis was conducted using Tikhonov regularization with a regularization parameter of 10^{-5}, implemented through the DRTtools framework developed by Wan [51].

3. Modeling

In an SOFC, hydrogen is supplied to the anode, while oxygen, often from the ambient air, is delivered to the cathode through the flow channels. At the cathode, oxygen molecules are reduced to negatively charged oxygen ions, which are transported across the solid electrolyte to the anode. At the anode, oxygen ions participate in the electrochemical oxidation of hydrogen, forming water and liberating electrons that travel through the external circuit to the cathode [52]. The corresponding half-cell electrochemical reactions for the solid oxide cell are listed below [53]:

$$H_2 + O^{2-} \rightarrow H_2O + 2\,e^- \tag{1}$$

$$\frac{1}{2}O_2 + 2\,e^- \rightarrow O^{2-} \tag{2}$$

3.1. Governing Equations

The SOFC was simulated using a 0-D, single-phase, steady-state, and non-isothermal model. The model incorporates electrochemical reactions as well as mass, heat, and charge transport, as depicted in Figure S1. The cell performance was calculated using the governing equations based on the Butler–Volmer relationship, Fick's law, and Ohm's law to capture kinetics, gas diffusion, and charge transport, respectively. The analytical model was developed using Python 3.11.4. The subsequent sections describe the mathematical formulation of the model, along with the associated parameters and implementation approach. The determination of all model parameters was primarily based on open-circuit conditions, except for the charge-transfer coefficients (α_{FE} and α_{AE}), which were calculated from impedance measurements under load. Electrochemical impedance measurements, combined with the distribution of relaxation times (DRT), were employed to resolve the individual polarization and transport losses and to examine their sensitivity to operating conditions. Distinct features observed in the DRT spectra, together with their characteristic responses to variations in operating parameters, were used to establish a linearized equivalent-circuit model (ECM) representation. Fitting of this model enabled the extraction of key material and kinetic properties, such as the ionic conductivity of the electrolyte, activation energy, exchange current density, and effective gas diffusion coefficients (D_i^{eff}).

3.1.1. Reversible Potential

The operating cell voltage (V_{cell}) was obtained by accounting for activation (η_{act}), ohmic (η_{ohm}), and concentration losses (η_{conc}), which were subtracted from the reversible potential E_{rev}, as expressed in Equation (3):

$$V_{\mathrm{cell,SOFC}} = E_{\mathrm{rev}} - \eta_{\mathrm{act}} - \eta_{\mathrm{ohm}} - \eta_{\mathrm{conc}} \tag{3}$$

The reversible potential E_{rev} [V] was calculated from the Nernst equation [54]:

$$E_{\mathrm{rev}} = -\frac{\Delta\hat{G}}{nF} + \frac{\Delta\hat{S}^0}{nF}(T - T_{\mathrm{ref}} + \frac{\Delta\hat{C}_p^0}{nF}\left[T\ln\left(\frac{T}{T_{\mathrm{ref}}}\right) - (T - T_{\mathrm{ref}})\right] - \frac{RT}{nF}\ln\left[\frac{P_{H_2O}}{P_{H_2}\left(\frac{P_{O_2}}{P_{\mathrm{ref}}}\right)^{0.5}}\right] \tag{4}$$

where $\Delta\hat{G}$ [J/mol], $\Delta\hat{S}$ [J/(mol·K)], and $\Delta\hat{C}_p$ [J/(mol·K)] represent the changes in Gibbs free energy, entropy, and specific heat capacity at constant pressure at the reference temperature and pressure, respectively. n denotes the number of electrons transferred, F [C/mol] is Faraday's constant, T [K] is the absolute operating temperature, and T_{ref} [K] is the reference temperature (298.15 K). R is the universal gas constant. P_{H_2}, P_{O_2}, and P_{H_2O} [kPa] are the supplied pressures of hydrogen, oxygen, and water vapor, respectively, while P_{ref} is the reference pressure (1 atm).

3.1.2. Activation Overpotential

The activation overpotential arises from the energy barriers that must be overcome for electrochemical reactions to proceed. In this model, the activation overpotential (η_{act}) represents the activation loss associated with HOR at the fuel electrode (FE) and ORR at the air electrode (AE). The gas concentrations used in these calculations correspond to the supplied gas compositions.

$$\eta_{\mathrm{act}} = \eta_{\mathrm{act,FE}} + \eta_{\mathrm{act,AE}} \tag{5}$$

The Butler–Volmer equation establishes the relation between the reaction rate and the activation overpotential for both the fuel-side HOR and the air-side ORR [55].

$$j = j_{0,\mathrm{FE/AE}}\left[\exp\left(\frac{\alpha_{\mathrm{FE/AE}} z_{\mathrm{FE/AE}} F \eta_{\mathrm{act}}}{RT}\right) - \exp\left(-\frac{(1-\alpha_{\mathrm{FE/AE}}) z_{\mathrm{FE/AE}} F \eta_{\mathrm{act}}}{RT}\right)\right] \tag{6}$$

where $j_{0,\mathrm{FE/AE}}$ [A/cm^2] represents the exchange current density on the fuel and air electrodes. $\alpha_{\mathrm{FE/AE}}$ is the charge-transfer coefficient and indicates the comparative magnitudes of the activation barriers for the forward and reverse reactions at the interface [25]. $z_{\mathrm{FE/AE}}$ represents the number of electrons transferred (specifically, $z_{\mathrm{FE}} = 2$ and $z_{\mathrm{AE}} = 4$). A common modeling assumption is to adopt a symmetric charge-transfer coefficient, $\alpha_{\mathrm{FE/AE}} = 0.5$, within a Butler–Volmer-type formalism [56]. The corresponding expressions for $j_{0,\mathrm{FE}}$ and $j_{0,\mathrm{AE}}$, together with their parameter definitions [57,58], are provided in the Supplementary Materials (Section S2).

3.1.3. Ohmic Overpotential

Ohmic losses originate from resistances associated with both electronic and ionic transport. These include bulk and contact resistances arising from electron conduction through the electrodes, interlayers, and current collectors, as well as ionic resistance associated with oxide ion transport across the multilayer electrolyte, consisting of YSZ, GDC, and the GDC/YSZ interdiffusion zone [59–63]. The resulting ohmic overpotential, η_{ohm}, can be expressed using Ohm's law as follows:

$$\eta_{\text{ohm}} = j \cdot \text{ASR}_{\text{ohm}} \tag{7}$$

where j is the operating current density and ASR_{ohm} represents the combined effective area-specific resistance.

In an SOFC, the ohmic resistance is predominantly governed by ionic conduction within the electrolyte layer. Under the assumption that electronic and contact resistances are negligible, the electrolyte ohmic overpotential can be approximated as follows [31]:

$$\eta_{\text{ohm}} = j\left(\frac{L_e}{\sigma_{\text{ionic,e}}}\right) \tag{8}$$

where L_e is the effective electrolyte thickness and $\sigma_{\text{ionic,e}}$ denotes the temperature-dependent effective ionic conductivity. Equation (8) represents an effective formulation intended to illustrate Ohm's law. Although ionic transport occurs through a three-layer structure comprising YSZ, GDC, and a GDC/YSZ interdiffusion zone with distinct conductivities, the resulting non-idealities are incorporated into an effective ohmic resistance rather than resolved as separate layers. The influence of the interdiffusion zone and interfacial contact losses is therefore captured implicitly through model validation against experimental electrochemical performance. A more detailed discussion of ohmic losses is provided in Section 3.2.5.

3.1.4. Concentration Overpotential

The concentration overpotential results from deviations between bulk gas composition and local TPB concentrations. While these concentrations are identical under open-circuit conditions, electrochemical operation induces gradients due to reactant consumption and product formation. Gas transport within the electrode pores, dissolution of reactants and products into and out of the electrolyte, and species diffusion collectively govern concentration polarization, which becomes more pronounced at higher current densities. The concentration overpotential is calculated using the following relations:

$$\eta_{\text{conc}} = \eta_{\text{conc,thermo}} + \eta^{\text{FE}}_{\text{conc,kinetic}} + \eta^{\text{AE}}_{\text{conc,kinetic}} \tag{9}$$

$$\eta_{\text{conc,thermo}} = \frac{RT}{z_{\text{FE}}F}\ln\left[\frac{P^{\text{CH}}_{\text{H}_2}P^{\text{TPB}}_{\text{H}_2O}}{P^{\text{TPB}}_{\text{H}_2}P^{\text{CH}}_{\text{H}_2O}}\left(\frac{P^{\text{CH}}_{\text{O}_2}}{P^{\text{TPB}}_{\text{O}_2}}\right)^{0.5}\right] \tag{10}$$

The thermodynamic concentration loss describes the overpotential arising from concentration differences between the gas channel and the triple-phase boundary (TPB), as described by the Nernst equation. The channel partial pressures, P^{CH}, are determined from the supplied gas composition, while the TPB partial pressures are obtained from steady-state mass conservation combined with Fickian diffusion [64]. The governing equations for the fuel and air electrodes, together with the resulting expressions for the TPB partial pressures $P^{\text{TPB}}_{\text{H}_2}$, $P^{\text{TPB}}_{\text{H}_2\text{O}}$, and $P^{\text{TPB}}_{\text{O}_2}$, are provided in the Supplementary Materials (Equations (S5)–(S9)). Meanwhile, concentration overpotential due to activation can be summarized as follows:

$$\eta_{\text{conc},KE} = \eta^{\text{TPB}}_{\text{act}} - \eta^{\text{AE/FE}}_{\text{act}} \tag{11}$$

Incorporating Equations (S1)–(S3) into Equation (11) yields explicit expressions for the kinetic concentration overpotentials at both electrodes.

3.1.5. Heat Transport

For a solid oxide cell, the total heat generation per unit area is given by [65]

$$q''_{\text{total}} = \left(\frac{|\Delta H|}{2F} - V_{\text{cell}} \right) \times i \tag{12}$$

where ΔH denotes the enthalpy change of the overall reaction. Heat is generated at the electrode surfaces due to electrochemical overpotentials, while additional Joule heating arises from electronic and ionic transport under load. Accordingly, heat dissipation is assumed to occur in three primary regions: the anode, the cathode, and the electrolyte. Temperature distributions are obtained by applying energy conservation and solving the resulting differential equations, accounting for reaction enthalpy and heat conduction, which are assumed to dominate thermal transport. The governing energy conservation equation for a porous medium is expressed as follows:

$$\frac{\partial}{\partial x} \left(k_{\text{i}} \frac{\partial T}{\partial x} \right) + \dot{q} = 0 \tag{13}$$

where k_i [W/mK] denotes the effective thermal conductivity of the solid parts of the cell, with reported values available in the literature [66]. The volumetric heat source, $\dot{q}$ [W/m^3], represents the irreversible heat generation due to charge transport as well as electrochemical reactions occurring in the electrodes.

As illustrated in Figure S2, a mass balance loop is used for the non-isothermal heat transfer calculations. Heat transfer perpendicular to the fuel cell plane can then be represented by a network of thermal resistances arranged in series. These conduction paths include both bulk conduction through solid domains and contact resistance at interfaces. In particular, interfacial joints such as those between the porous Ni mesh and the SOFC anode (Ni–YSZ) ($R_{\text{th},c1}$), as well as between the cathode and the Pt mesh and interconnector ($R_{\text{th},c2}$), play a dominant role. The resistance values were obtained from experimental data at 650 °C and 800 °C using linear fitting of reported measurements for the anode side, and for the cathode side they were estimated based on [67]. Accordingly, the thermal contact resistances were determined as $R_{\text{th},c1} = 5.87 \times 10^{-2}$ cm^2 K W^{-1} and $R_{\text{th},c2} = 1.032 \times 10^{-1}$ cm^2 K W^{-1}.

3.2. SOFC Model Parameter Extraction from EIS and DRT Analysis

DRT analysis resolved four primary relaxation features (P_1–P_4) in the SOFC spectra (Figures 2). The low-frequency feature P_1, with its associated resistance R_1, was attributed to gas conversion effects. It should be emphasized that this process is not intrinsic to the electrochemical cell itself but, rather, arises from the test-bench configuration and the low gas flow rate employed (100 sccm) [24], under which fuel depletion and gas composition changes along the flow field become significant. The intermediate-frequency feature P_2 corresponds to gas-transport-related processes. The higher-frequency features (P_3 and P_4) can be attributed to electrode polarization phenomena. Following a more detailed interpretation reported by Grosselindemann et al. [45], P_1 (<1 Hz) primarily arises from fuel-side gas conversion under low-flow-rate conditions. In contrast, P_2 (∼10 Hz) can be attributed to gas diffusion limitations within the Ni-YSZ anode substrate at the fuel side, with the associated resistance denoted as R_2. This process reflects concentration polarization arising from gas transport through the porous anode support rather than intrinsic electrochemical kinetics. The higher-frequency features P_3 and P_4 likely reflect overlapping contributions from electrochemical processes occurring at both the air and fuel electrodes.

Impedance spectra were analyzed using complex nonlinear least-squares fitting implemented in EC-Lab software (v11.50) The ECM was constructed based on the dominant relaxation features identified from DRT analysis. Figure 2 illustrates the impedance spectrum acquired at 700 °C and 100% O_2 under open-circuit conditions, together with the corresponding DRT spectrum and the fitted ECM response. Although the Nyquist plot exhibits overlapping arcs that obscure direct process identification, the DRT analysis resolves four distinct relaxation peaks (P_1–P_4), each associated with a dominant electrochemical process. These features guided the selection and arrangement of circuit elements, with the first element representing the ohmic resistance and the remaining processes modeled using RQ elements, whose physical significance was inferred from their characteristic frequency ranges and systematic response to operating conditions.

As evident in Figure 2, the Nyquist semicircles appear flattened. This behavior results partly from the disproportionate compression of the imaginary axis relative to the real axis, and partly from intrinsic non-ideal relaxation behavior. As described in Refs. [68–70], the impedance responses of real electrochemical systems arise from a superposition of processes with distinct time constants. Replacing an ideal capacitor with a constant-phase element (CPE) introduces a dispersion exponent $n_{RQ} < 1$, which broadens and flattens the semicircle. In this study, the fitted CPE exponents range from 0.50 to 1.0.

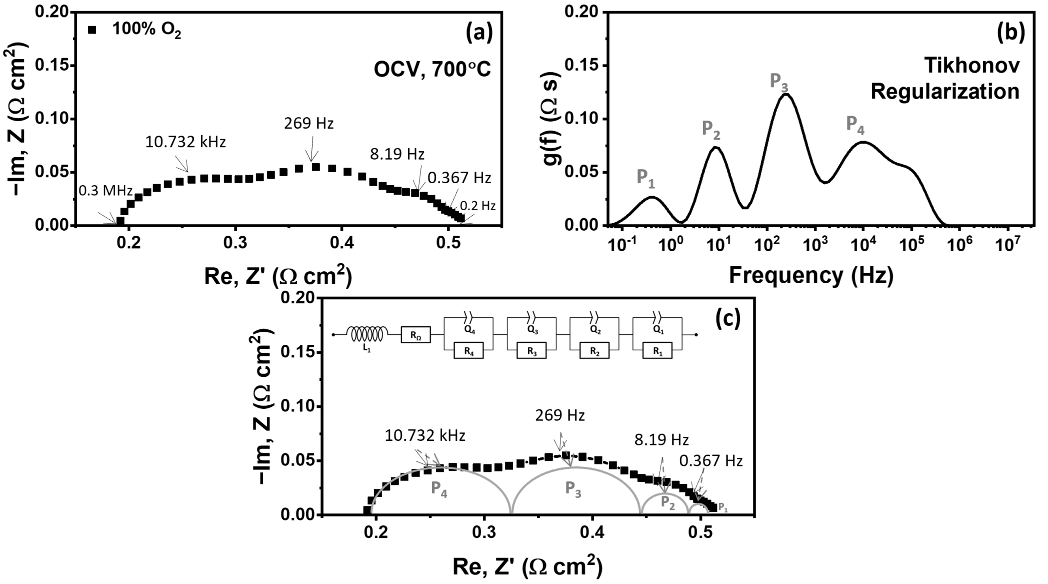

Figure 2. (**a**) Impedance spectrum measured at 700 °C, 100% H_2, and 100% O_2 at OCV, with peak frequencies identified from the DRT spectrum; (**b**) the corresponding DRT showing four resolved processes; and (**c**) EIS fit using the ECM constructed from the DRT assignments.

3.2.1. Activation Overpotential Exponent Parameters a, b, and m

This step determines the parameters required to estimate the activation overpotential. To calculate the exponents a and b, the concentrations and partial pressures of hydrogen and water were varied independently while maintaining a constant temperature. The combined use of impedance spectroscopy and an ECM enables evaluation of the anode activation polarization resistance as a function of the partial pressures of hydrogen and steam under OCV conditions.

In this study, the value of a was adopted from the literature. However, the exponent b was estimated by varying the water concentration in the fuel electrode under reversible solid oxide cell (SOC) mode, assuming constant $a = -0.1$ [39] and a hydrogen concentration defined as $x_{H_2} = 1 - x_{H_2O}$ at OCV.

Equation (14) outlines how the exchange current density correlates with the activation resistance:

$$\left.\frac{d\eta_{\mathrm{act,AE/FE}}}{dj}\right|_{j=0} = \frac{RT}{z_{\mathrm{AE/FE}}Fj_{0,\mathrm{AE/FE}}} = ASR_{\mathrm{act,AE/FE}} \tag{14}$$

The parameter b is determined by fitting the impedance-derived values of $R_{\mathrm{act,FE}}$. The full analytical form of the fuel-side activation resistance, derived by substituting Equation (S1) into Equation (14), is presented in Equation (S3). The impedance spectra and their corresponding DRTs are shown in Figure 3 for reversible SOEC measurements at controlled water vapor pressures of 50 kPa, 30 kPa, and 3 kPa.

Based on DRT deconvolution and equivalent-circuit fitting of the EIS data, the resistances R_3 and R_4 were extracted under open-circuit conditions. The corresponding DRT features, P_3 and P_4, modeled using two RQ elements, were attributed to fuel-electrode activation processes associated with charge transfer at the triple-phase boundaries and oxygen-ion conduction within the YSZ matrix of the anode functional layer during the H_2/H_2O redox reaction. Accordingly, the combined resistance $R_3 + R_4$ was defined as the fuel-side activation resistance, $R_{\mathrm{act,FE}}(P_{\mathrm{H_2}O}/P_{\mathrm{ref}})$, and was analyzed as a function of water partial pressure. The water vapor pressures used in this analysis correspond to the leakage-corrected, OCV-derived equilibrium values presented in Table S3, rather than nominal inlet conditions, ensuring a physically consistent interpretation of the pressure-dependent activation behavior.

Figure 3 presents a log–log analysis of R_3 as a function of $P_{\mathrm{H_2O}}/P_{\mathrm{ref}}$, revealing an inverse power-law dependence consistent with the adopted semi-empirical model. The corresponding slope, denoted b, was extracted at each operating temperature. At 700, 660, and 620 °C, the slopes were comparable, yielding an average value of $b \approx 0.338$. In contrast, the slope at 580 °C was markedly lower ($b = 0.0497$), indicating a significant deviation from this trend. As shown in Figure 3i, the 580 °C data exhibit a noticeably flatter slope, reflecting a weaker dependence on steam's partial pressure. A similar behavior is observed in the Arrhenius representation (Figure 3j), where the 580 °C data cluster across all steam concentrations, indicating minimal variation in R_3. This convergence suggests that alternative rate-limiting mechanisms, such as modified electrode kinetics, mass transport limitations, or steam adsorption effects, may dominate at lower temperatures. Consequently, the 580 °C dataset was excluded from the calculation of the average b value used in subsequent analyses.

A similar analysis was applied to the air electrode to determine the exponent m, which characterizes the dependence of cathodic activation polarization on the partial pressure of oxygen at constant temperature. Impedance spectra collected under varying $P_{\mathrm{O_2}}/P_{\mathrm{ref}}$ conditions reveal the sensitivity of air-electrode kinetics to oxidant availability, with the corresponding DRT results shown in Figure 4. Among the resolved features, P_3 exhibits the strongest dependence on oxygen's partial pressure, indicating its association with surface oxygen exchange and oxygen-ion diffusion within the air electrode. The corresponding resistance R_3 therefore represents cathodic polarization losses dominated by oxygen incorporation and transport rather than gas-phase diffusion. Following the same procedure used to extract the fuel-side exponent b, the air-electrode reaction order m was obtained by fitting impedance-derived activation resistance data to a logarithmic model, with the full formulation provided in the Supplementary Materials.

Figure 4 shows that, in addition to P_3, the DRT features P_1, P_2, and P_4 also shift with increasing partial pressure of oxygen. Such behavior is consistent with the strongly coupled nature of electrochemical and transport processes in SOFC electrodes, in which variations in oxygen activity can simultaneously affect multiple impedance contributions [71]. Additional shifts may also originate from parasitic phenomena, including oxygen crossover or gas leakage from the air to the fuel electrode, particularly under non-ideal contact conditions [72,73]. Elevated P_{O_2}/P_{ref} is known to enhance leakage, potentially influencing impedance features over a broad frequency range; this effect was qualitatively assessed by comparing theoretical and measured open-circuit voltages. Despite these coupled responses, the cathodic reaction order m was extracted based on the dominant oxygen sensitivity of P_3, while the multi-peak response reflects non-ideal impedance behavior under these conditions. The fitted value, $m = 0.236$, obtained from the logarithmic dependence of $ASR_{\mathrm{act,AE}}$ on oxygen's partial pressure (Figure 4i,j), indicates a strong dependence of air-electrode kinetics on local oxygen availability. This result complements the fuel-side analysis and highlights asymmetric kinetic behavior between the electrodes.

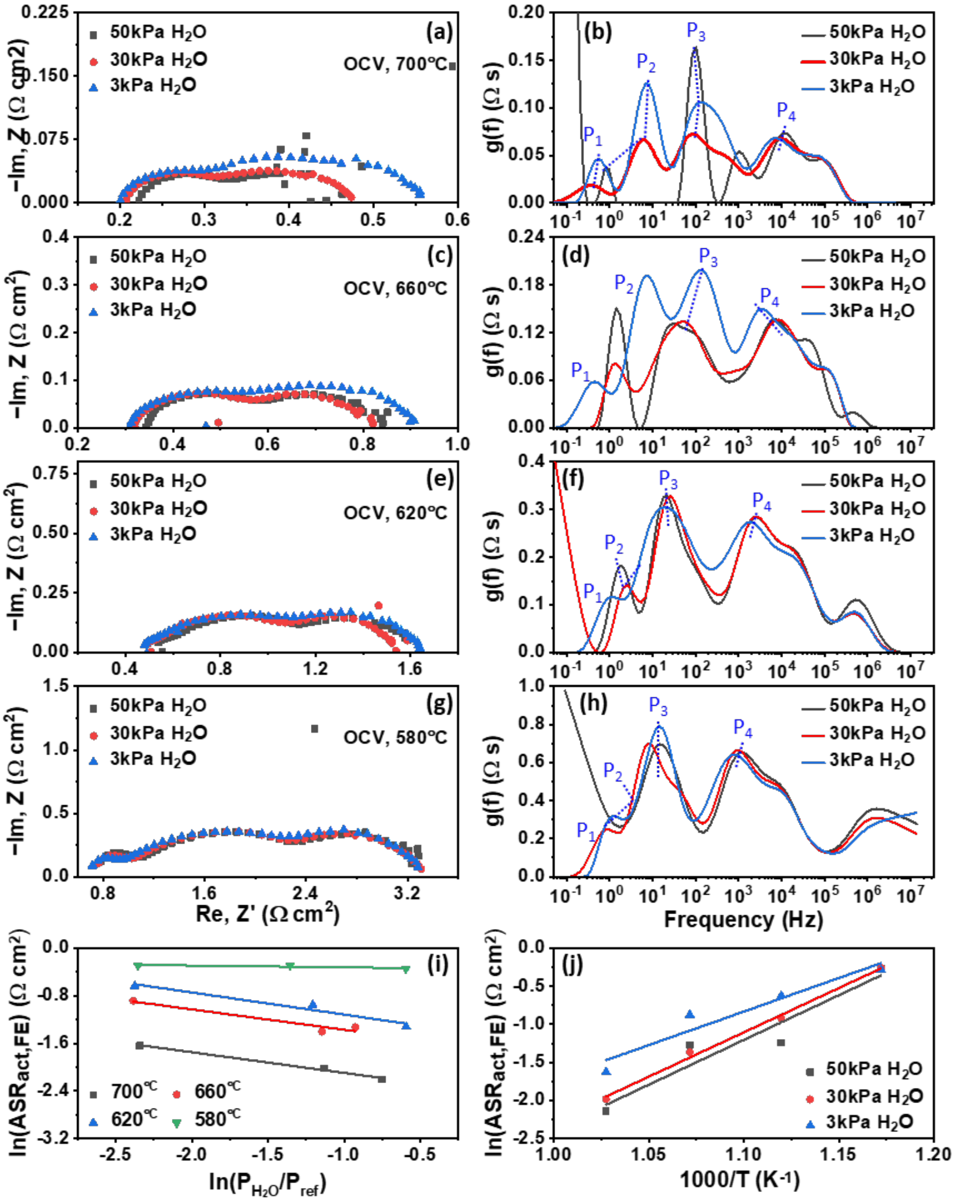

Figure 3. EIS spectra and corresponding DRTs from reversible SOC experiments at 700 °C (**a**,**b**), 660 °C (**c**,**d**), 620 °C (**e**,**f**), and 580 °C (**g**,**h**) under controlled vapor fractions $P_{H_2O}^{\mathrm{FE}}/P_{\mathrm{ref}} = \{0.03, 0.3, 0.5\}$ and $P_{O_2}^{\mathrm{FE}}/P_{\mathrm{ref}} = \{0.21\}$. (**i**) Determination of parameter ’b′. $\ln ASR_{\mathrm{act,FE}}$ $[\Omega \cdot \mathrm{cm}^2]$ as a function of vapor partial pressures obtained from OCV values, $\ln(P_{H_2O}^{FE}/P_{\mathrm{ref}})$. (**j**) Determination of the fuel-electrode activation energy $E_{\mathrm{act,FE}}$ in Equation (15).

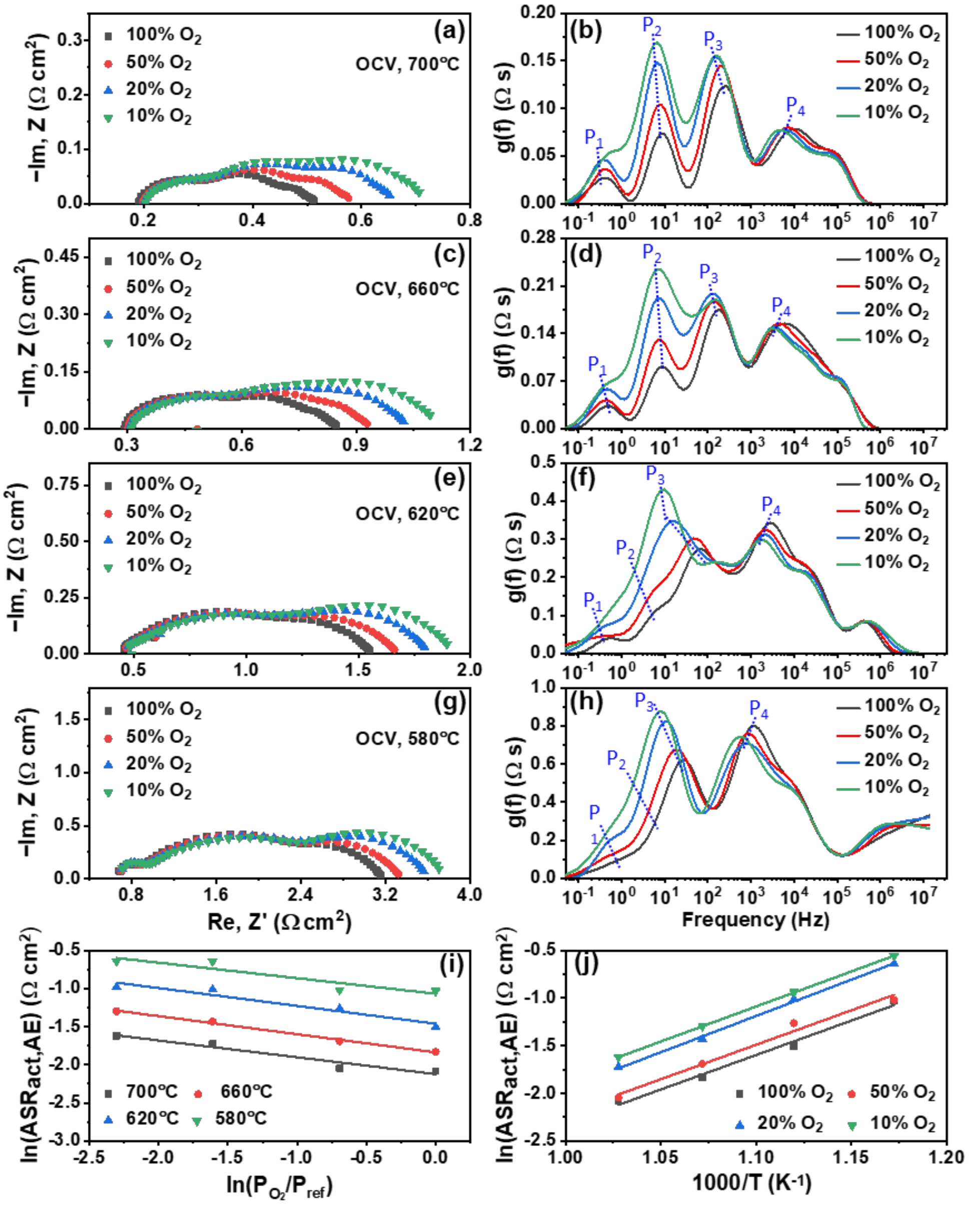

Figure 4. EIS spectra and corresponding DRTs from SOFC experiments at 700 °C (**a**,**b**), 660 °C (**c**,**d**), 620 °C (**e**,**f**), and 580 °C (**g**,**h**) for $P_{O_2}^{AE}/P_{ref} = \{0.1, 0.2, 0.5, 1\}$ and $P_{H_2}^{AE}/P_{ref} = \{1\}$. (**i**) Determination of parameter 'm' at different oxygen concentrations ($P_{O_2}^{AE}/P_{ref}$ = 0.1, 0.2, 0.5, 1). (**j**) Determination of the air-electrode activation energy $E_{act,AE}$, based on DRT peak shifts extracted from the EIS spectra.

3.2.2. Activation Energies and Pre-Exponential Parameters γ_{FE} and γ_{AE}

The calculation of the kinetic activation energies $E_{act,FE}$ and $E_{act,AE}$, along with the parameters γ_{FE} and γ_{AE}, as described in Equations (S1) and (S2), requires impedance measurements under OCV conditions at different operating temperatures while maintaining a fixed gas composition. In this context, the DRT results shown in Figures 3 and 4 were used to extract the activation polarization resistance from the EIS regression of the corresponding impedance spectra. Subsequently, the temperature-dependent resistances were fitted to the Arrhenius equation to determine the kinetic parameters.

$$ASR_{act,AE/FE}(T) = B_{AE/FE} \cdot \exp\left(\frac{E_{act,\,AE/FE}}{RT}\right) \tag{15}$$

The temperature-dependent air-electrode activation resistance, $ASR_{\text{act,AE}}(T)$, was obtained by isolating the electrochemical process associated with Peak 3 in the DRT analysis. Linear regression of the temperature-dependent resistance yielded the cathode activation energy and pre-exponential factor for each oxygen concentration. The air electrode exhibited an activation energy of $E_{\text{act,AE}} = 116.8\,\text{kJ/mol}\,(1.21\,\text{eV})$, along with a concentration-dependent pre-exponential factor B_{AE}, as listed in Table S1. The reported activation energies for SOFC systems typically fall in the range of 0.7–3 eV [74–80]. In this study, the cathodic pre-exponential factor γ_{AE} was found to scale linearly with temperature and was approximated as $\gamma_{\text{AE}} \approx 7.1 \times 10^3 T$ over the investigated oxygen concentrations, indicating that the temperature dependence of the cathode kinetics is primarily captured through this proportionality.

$$\gamma_{AE} = \frac{RT}{2FB_{AE}}\left(\frac{P_{O_2}}{P_{\text{ref}}}\right)^{-m} \tag{16}$$

The same procedure was used to determine the fuel-electrode activation energy, $E_{\text{act,FE}}$. As illustrated in Figure 3j, the 580 °C data exhibit pronounced clustering at low steam fractions, resulting in minimal resistance variation and an anomalously low Arrhenius slope. Consequently, the activation energy extracted at 3% H_2O can be considered an outlier. This behavior suggests a decoupling of the expected kinetic response from steam's partial pressure, likely due to suppressed surface exchange or dominant diffusion limitations under low-hydration and low-temperature conditions. Therefore, only data obtained at higher steam contents (30% and 50% H_2O) were used to determine the effective Eact, FE, ensuring consistency with the pressure-dependence trends observed at higher temperatures. This yielded a representative activation energy of $E_{\text{act,FE}} = 99.857$ kJ.mol^{-1} (1.035 eV), which falls within the reported range of 70–189 kJ.mol^{-1} for Ni-based anodes [81–90]. A concentration-dependent pre-exponential factor B_{FE} was obtained accordingly, as summarized in Table S2. The temperature-scaled pre-factor for the fuel electrode, γ_{FE}, was subsequently derived as follows:

$$\gamma_{\text{FE}} = \frac{RT}{2FB_{\text{FE}}}\left(\frac{P_{H_2}}{P_{\text{ref}}}\right)^{-a}\left(\frac{P_{H_2O}}{P_{\text{ref}}}\right)^{-b} \tag{17}$$

Analogous to the air-electrode formulation, this expression confirms that γ_{FE} exhibits a linear dependence on temperature. To ensure consistency with the kinetic trends observed at higher steam contents, only the fitted B_{FE} values obtained at 30% and 50% H_2O were included, while the 3% H_2O case was excluded due to its previously noted deviation from Arrhenius behavior. Based on the averaged values in Table S3, the exchange current density pre-factor was approximated as $\gamma_{\text{FE}} \approx 1.0227 \times 10^5 T\ [\text{A/m}^2]$.

3.2.3. Charge-Transfer Coefficients, α_{FE} and α_{AE}

Impedance measurements under load conditions were employed to determine the charge-transfer coefficients for the anode and cathode, denoted as α_{FE} and α_{AE}, respectively. These experiments were performed at fixed partial pressures of $P_{H_2,\text{FE}} = 1$ atm and $P_{O_2,\text{AE}} = 1$ atm, across operating temperatures of 700 °C, 660 °C, 620 °C, and 580 °C. EIS spectra were collected under varying load conditions.

To determine the charge-transfer coefficient, α_{el}, for both electrodes, the differential activation resistance under load conditions was extracted from the DRT analysis. Specifically, the resistance associated with Peak 3 was used for the air electrode based on SOFC EIS spectra, while the same relaxation feature was analyzed for the fuel electrode using SOEC EIS spectra. This peak can be attributed to electrode activation polarization dominated by charge-transfer and surface-reaction kinetics, as expressed by

$$dR_{\mathrm{act,AE/FE}} = \frac{d\eta_{\mathrm{act,AE/FE}}}{dj} \tag{18}$$

The corresponding current densities j at each applied voltage were then calculated, and the relationship between $dR_{\mathrm{act,AE/FE}}$ and j was fitted using a second-order polynomial:

$$dR_{\mathrm{act,AE/FE}}(j) = aj^2 + bj + c \tag{19}$$

The estimated $\eta_{\mathrm{act,AE/FE}}(j)$ values were then fitted using the Tafel equation to obtain the charge-transfer coefficient:

$$\eta_{\mathrm{act,AE/FE}}(j) = \frac{RT}{\alpha z F} \ln\left(\frac{j}{j_0}\right) \tag{20}$$

Figure 5a presents the EIS spectra collected under varying voltage loads at 700 °C, while Figure S3 shows the complete set of EIS spectra acquired under load at different temperatures, highlighting the changes in impedance response with increasing current density. Figure 5b displays the corresponding DRTs, where the peak evolution under load provides insights into the electrode-specific polarization behavior. Figure 5c shows the extracted differential activation resistances, $dR_{\mathrm{act,AE}}$ and $dR_{\mathrm{act,FE}}$, plotted against the current density j. From this analysis, the charge-transfer coefficients were determined to be $\alpha_{\mathrm{FE}} = 0.65$ for the fuel electrode and $\alpha_{\mathrm{AE}} = 0.46$ for the air electrode.

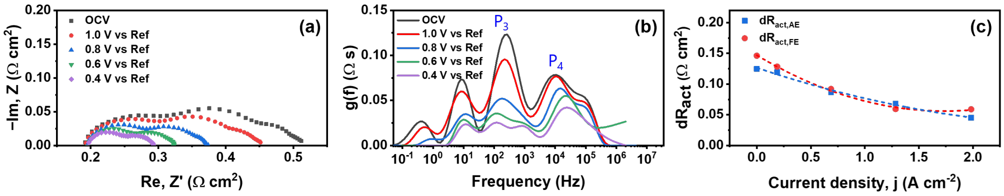

Figure 5. Determination of the charge-transfer coefficients α_{an} and α_{cat}: (**a**) EIS spectra measured at various cell voltages ($V = 0.4, 0.6, 0.8, 1.0$ V, and OCV) under $P_{\mathrm{H_2,FE}}/P_{\mathrm{ref}} = 1$ atm and $P_{\mathrm{O_2,AE}}/P_{\mathrm{ref}} = 1$ atm, and at $T = 700$ °C; (**b**) corresponding DRTs; (**c**) $dR_{\mathrm{act,AE}}$ and $dR_{\mathrm{act,FE}}$ $[\Omega \cdot \mathrm{cm}^2]$ plotted against current density j, along with corresponding second-order polynomial fits.

3.2.4. Ohmic Resistance and Ionic Conductivity

Ohmic resistance values were obtained from the high-frequency intercepts of the Nyquist plots under OCV conditions. Ionic conductivity was then derived from the extracted $\mathrm{ASR_{ohm}}$ values using an Arrhenius-type model. A simplified ECM, consisting of an inductance (L_1) and a resistance (R_1) element, was employed for fitting. The fitted ohmic resistance values across temperatures and oxygen conditions, presented in Figure 4, are listed in Table S4. The pronounced linearity observed in the Arrhenius plot (Figure 6) confirms the thermally activated nature of ionic conduction. Regression analysis yielded adjusted R^2 values exceeding 0.998 for all oxygen concentrations, indicating an excellent fit to the Arrhenius relationship. Following the extraction of $\mathrm{ASR_{ohm}}$, the ionic conductivity of the electrolyte at each temperature was calculated using

$$\sigma_{\mathrm{ionic,e}}(T) = \frac{L_e}{\mathrm{ASR_{ohm}}(T)} \tag{21}$$

where L_e is the known electrolyte thickness. The ionic conductivity exhibits an Arrhenius-type temperature dependence, increasing with temperature due to enhanced ion mobility within the dense electrolyte layer. The temperature dependence of the extracted $\mathrm{ASR_{ohm}}$ values was fitted to an Arrhenius-type relationship [91,92]:

$$\sigma_{\text{ionic,e}}(T) = \frac{A_{\text{ohm}}}{T} \exp\left(\frac{-E_{\text{act, ohm}}}{RT}\right) \tag{22}$$

where parameters A_{ohm} (cell-specific constant) and $E_{\text{act, ohm}}$ (activation energy for ionic conduction) were determined, yielding the following fitting results:

$$A_{\text{ohm}} = 105,303\,\text{S} \cdot \text{K/cm}, \quad E_{\text{act, ohm}} = 79.944\,\text{kJ/mol}\,(0.829\,\text{eV})$$

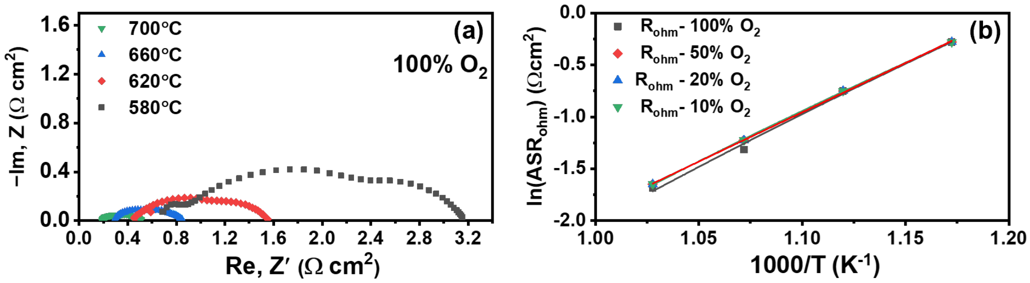

Figure 6. (**a**) EIS spectra for 100% O_2 and 100% H_2 at 580, 620, 660, and 700 °C. (**b**) Determination of the ohmic resistance, ASR_{ohm} $[\Omega \cdot \text{cm}^2]$, from EIS data fitting at 580, 620, 660, and 700 °C for 100%, 50%, 30%, and 10% O_2 and 100% H_2; and estimation of the parameters A_{ohm} and $E_{\text{act,ohm}}$ at different O_2 concentrations by fitting Equation (22).

3.2.5. Non-Ideal Ohmic Losses and Interfacial Resistances

In practice, the experimentally measured high-frequency intercept (R_{ohm}) cannot fully capture the non-ideal losses present in the cell. To reconcile the model predictions with the impedance measurements under all operating conditions, an additional lumped ohmic contribution was considered, accounting for interfacial and contact resistances at the current collectors, electrode–electrolyte interfaces, and geometric constriction effects within porous electrodes. These contributions are not intrinsic material properties of the electrolyte but represent unavoidable non-idealities and are therefore incorporated as an effective ohmic resistance in the analysis. These contributions include (i) contact resistances between the porous materials and the current collector [93]; (ii) local degradation of electrolyte conductivity near the Ni–YSZ interface, caused by Ni diffusion under reducing conditions [94,95]; (iii) an interdiffusion zone resulting in low conductivity of the GDC layer [96]; and (iv) possible $SrZrO_3$ formation in the cathode/electrolyte interface region, which may further contribute to ohmic or polarization resistance, depending on its microstructure [97–99]. Similar situations are also documented in low-temperature fuel cells, where the catalyst layer's ionic resistance contributes to the total ohmic polarization [100,101]. In addition to these interfacial effects, a finite ionic conduction path may exist within the composite electrodes when the electronically conducting backbone (Ni or LSCF) becomes discontinuous due to agglomeration or microstructural degradation. To account for the cumulative effect of these processes, the total effective area-specific resistance is expressed as the sum of the electrolyte contribution and a residual non-ideal resistance term, as given in Equation (23). As shown in Figure 7, the effective total resistance increasingly deviates from the electrolyte contribution with decreasing temperature, highlighting the growing impact of non-ideal interfacial and contact resistances.

$$ASR_{\text{eff,tot}}(T) = \frac{L_{\text{e}}}{\sigma_{\text{ionic,e}}(T)} + \frac{L_{\text{eff}}}{\kappa(T)} \tag{23}$$

where $ASR_{\text{eff,tot}}$ denotes the effective total resistance, L_{e} is the electrolyte thickness, and $\sigma_{\text{ionic,e}}(T)$ is the electrolyte ionic conductivity derived in Section 3.2.4. Here, L_{eff} and

$\kappa(T)$ are empirical fitting parameters representing the aggregate interfacial and contact resistances. Unlike a physical conduction path, L_{eff} does not correspond to a measurable thickness but serves as a scaling factor linking the apparent interfacial area to the observed temperature dependence. The parameter $\kappa(T)$ follows an Arrhenius-type relation.

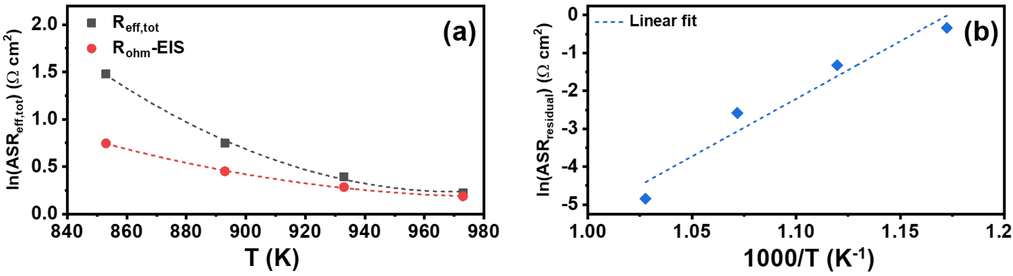

Figure 7. (**a**) Area-specific ohmic and total resistances based on non-idealities, showing the growing discrepancy between effective total resistance and the electrolyte contribution as temperature decreases. (**b**) Arrhenius plot of the residual non-ideal resistance contribution ($ASR_{\mathrm{residual}}(T)$); the linear fit yields a slope of 30.4357 with $R^2 = 0.944$, supporting the chosen $\kappa(T)$ model.

The detailed functional form of $\kappa(T)$ and the expression for the electrode's resistance contribution, $ASR_{\mathrm{residual}}(T)$, are provided in Equations (S19) and (S20). These relationships explain the observed sharp increase in electrode resistance at lower temperatures, emphasizing the importance of including this term when modeling SOFC ohmic losses at intermediate and low temperatures.

3.2.6. Structural Parameters, ψ_{FE} and ψ_{AE}

This section establishes a methodology for accurately extracting the structural parameters ψ_{FE} and ψ_{AE} from impedance spectroscopy data. These parameters are critical for quantifying the mass transport overpotential, thereby enabling a comprehensive characterization of the system's electrochemical behavior, especially at the mass transport region. To determine ψ_{FE} and ψ_{AE}, the humidity level at the fuel electrode and the oxygen concentration were varied. To quantify this contribution, the low-frequency diffusion resistance, $R_{\mathrm{diff,FE}}$, corresponding to mass transport limitations in the porous Ni/YSZ anode substrate, was isolated from the EIS spectra. To accurately capture its dependence on humidity and temperature, the concentration overpotential model for the fuel electrode was considered. Using the expressions for the concentration gradient and overpotential (Equations (S5)–(S16)) [102], the model was reformulated into an explicit expression for the diffusion resistance by linearization and rearrangement, yielding Equation (24). In this formulation, the porosity-to-tortuosity ratio, $\psi_{\mathrm{FE}} = \frac{\varepsilon_{\mathrm{FE}}}{\tau_{\mathrm{FE}}}$, was treated as an unknown fitting parameter to be extracted from experimental data.

$$R_{\mathrm{diff,FE}} = \left(\frac{RT}{2F}\right)^2 \frac{L_{\mathrm{FE}}}{\psi_{\mathrm{FE}}} \frac{1}{D_{\mathrm{H_2O-H_2}}} \left(\frac{1}{p_{\mathrm{H_2O}}} + \frac{1}{1 - p_{\mathrm{H_2O}}}\right) \frac{1}{P_{\mathrm{corr}}} \tag{24}$$

where P_{corr} is a correction factor of 101,325 Pa/atm. At elevated temperatures (700 °C and 660 °C), the contribution of thermally activated polarization processes is significantly reduced, allowing a more direct assessment of diffusion-related resistances. Under these conditions, the extracted values of $R_{2,\mathrm{FE}}$ are therefore predominantly governed by gas-phase transport through the anode substrate. To facilitate parameter extraction and trend analysis, Equation (24) was subsequently simplified into logarithmic form, resulting in the following proportional relationship:

$$ASR_{\mathrm{diff,FE}} = C\, P_{\mathrm{H_2O}}^{n} \tag{25}$$

where C is a fitting constant and n represents the power-law dependence of the diffusion resistance on the partial pressure of water vapor. Using least-squares fitting in logarithmic space, the experimentally extracted $ASR_{\mathrm{diff,FE}}$ data were fitted to the diffusion model derived from Fick's law, as given in Equation (25). From this fitting procedure, the porosity-to-tortuosity factor ψ_{FE} was extracted, providing quantitative insight into the microstructural characteristics of the fuel-electrode substrate. The extracted parameters, along with the corresponding porosity-to-tortuosity factors at each operating temperature, are presented in Figure 8 and Table 1. Averaging these values yields $\psi_{\mathrm{FE}} = 0.198$.

Table 1. Extracted slopes and porosity-to-tortuosity factors ψ_{FE} at different temperatures.

Temperature [°C]	$D_{\mathrm{H_2,H_2O}}$ **[cm^2· s^{-1}]**	C	**Slope (n)**	ψ_{FE}	$\psi_{\mathrm{FE,avg}}$
700	6.9619	0.01442	−0.496	0.18965	0.19793
660	6.4689	0.01427	−1.128	0.20620	

Note: $\psi_{\mathrm{FE,avg}}$ represents the average porosity-to-tortuosity factor calculated across both temperatures.

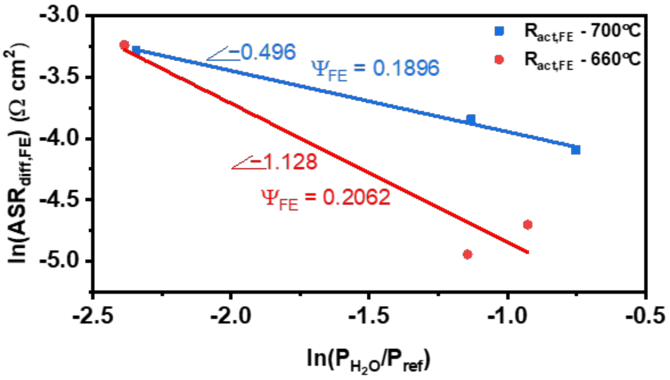

Figure 8. Fuel-electrode diffusion resistance from EIS regression: ASR$_{\mathrm{diff,FE}}$ at 660 and 700 °C, 50, 30, and 3 kPa H_2O and 21% O_2.

The full derivation and fitting procedure for the air-side diffusion resistance model are summarized in Table S5. The observed deviation between the extracted resistance values and those reported in the literature suggests that the resistance associated with the P_2 feature cannot be attributed to pure gas-phase diffusion alone. Instead, P_2 represents a lumped polarization process that incorporates gas transport within the porous LSCF-based electrode together with additional electrochemical contributions. This interpretation is further supported by the pronounced temperature dependence of the P_2 feature, which cannot be explained only by gas-phase diffusion mechanisms and instead indicates the involvement of thermally activated electrochemical processes. Such lumped behavior is consistent with previous studies on porous mixed ionic–electronic conductor (MIEC) cathodes, where mass-transfer-related impedance features were shown to overlap with surface oxygen exchange and bulk oxygen-ion diffusion processes. In these systems, oxygen transport is governed by coupled electrochemical and transport mechanisms that are more appropriately described by a Gerischer-type response rather than by a purely diffusive element. Consequently, the extracted ψ_{AE} values obtained by treating P_2 as a diffusion-dominated process cannot be interpreted as intrinsic indicators of the cathode's microstructural diffusion properties. In particular, the characteristic R_2 feature attributed to gas-phase diffusion in the LSCF electrode is convoluted with additional kinetic processes, leading to a systematic underestimation of the effective porosity-to-tortuosity factor when fitted directly from P_2, as illustrated in Figure S4.

An additional factor contributing to the underestimated ψ_{AE} values is the limited experimental resolution of gas-phase diffusion under the investigated partial pressure of oxygen range. Previous analyses of similar LSCF cathode structures have demonstrated that gas-phase diffusion can only be unambiguously resolved in the DRT spectrum at very low partial pressures of oxygen ($P_{O_2,\mathrm{AE}}/P_{\mathrm{ref}} < 0.05$) [39,45]. At higher oxygen concentrations, the diffusion-related contribution merges with adjacent electrochemical processes, further complicating the separation and promoting underestimation of ψ_{AE}. In the present study, the use of pure oxygen at the cathode further suppressed gas-phase diffusion [103] by minimizing oxygen concentration gradients within the porous electrode, making the appearance of a distinct diffusion-related DRT peak unlikely.

To avoid non-physical parameter compensation, and to ensure a realistic representation of air-electrode transport in subsequent modeling and analysis, a literature-based value of $\psi_{\mathrm{AE}} = 0.048$ reported by Grosselindemann et al. [45] was therefore adopted. This value is representative of comparable LSCF-based cathode microstructures and provides a physically consistent estimate for air-side mass transport under the present operating conditions. Thus, under ideal cathode contact conditions, the contribution of air-side gas diffusion to the overall SOFC performance is negligible. This is consistent with previous studies showing that, for well-contacted LSCF-based air electrodes, gas-phase diffusion becomes performance-relevant only at very low partial pressures of oxygen. Under an ideal small-scale single-cell configuration, air-side gas transport is not a dominant limitation for well-contacted LSCF-based cathodes. However, under a stack-like design employing a channel–rib flow-field, lateral oxygen transport beneath the cathode ribs can become significantly constrained. Multiphysics modeling of planar SOFC stacks has demonstrated that such in-plane transport limitations lead to oxygen depletion at cathode triple-phase boundaries beneath wide ribs, thereby increasing the cathode concentration polarization and degrading cell performance. Consequently, in these configurations, in-plane gas diffusion beneath air-side ribs may become performance-limiting [104,105]. Since the porosity and tortuosity of the air electrode in the present cell were not characterized in detail, and additional transport limitations may arise from the contacting configuration, the effective air-side gas diffusion resistance may be larger than that of an ideally contacted cathode.

4. Results

This section evaluates the model's predictive accuracy by comparing simulated polarization curves (I–V curves) to experimental measurements under varying partial pressures of oxygen and temperatures. As shown in Figure 9, the model captures performance trends across four oxygen concentrations (10%, 20%, 50%, and 100%) and four temperatures (580 °C, 620 °C, 660 °C, and 700 °C).

At higher temperatures, ohmic losses decrease due to enhanced ionic conductivity, consistent with Arrhenius behavior. A slight reduction in OCV is also observed, resulting from the thermodynamic shift in the Nernst potential. The model predicts limiting-current behavior at low partial pressures of oxygen, especially at 10% O_2 and 700°C, where cathodic diffusion limitations lead to a pronounced voltage drop at relatively low current densities.

Figure 10a presents the decomposition of each overpotential component as a function of the applied current density. Ohmic resistance becomes the dominant contribution at high current densities. Activation overpotentials, particularly for HOR, are significantly smaller. Contributions from ORR kinetics and gas diffusion are minor under the tested conditions but can increase under more oxygen-limited environments or stack-level configurations. To assess non-isothermal effects, the local temperature distribution at 1 and 2.2 A cm^{-2} is shown in Figure 10b. Although higher current density leads to a measurable increase in temperature, the maximum temperature difference across the cell remains below 1 K. This magnitude is comparable to the uncertainty range of industrial thermocouples, indicating that temperature gradients in the present cell configuration are negligible. Consequently, under the investigated operating conditions, the cell can be considered quasi-isothermal, and thermal non-uniformities are not expected to significantly influence the electrochemical response. Nonetheless, the non-isothermal framework provides a consistent basis for extending the model to larger-area cells or higher current densities, where thermal gradients may become more pronounced.

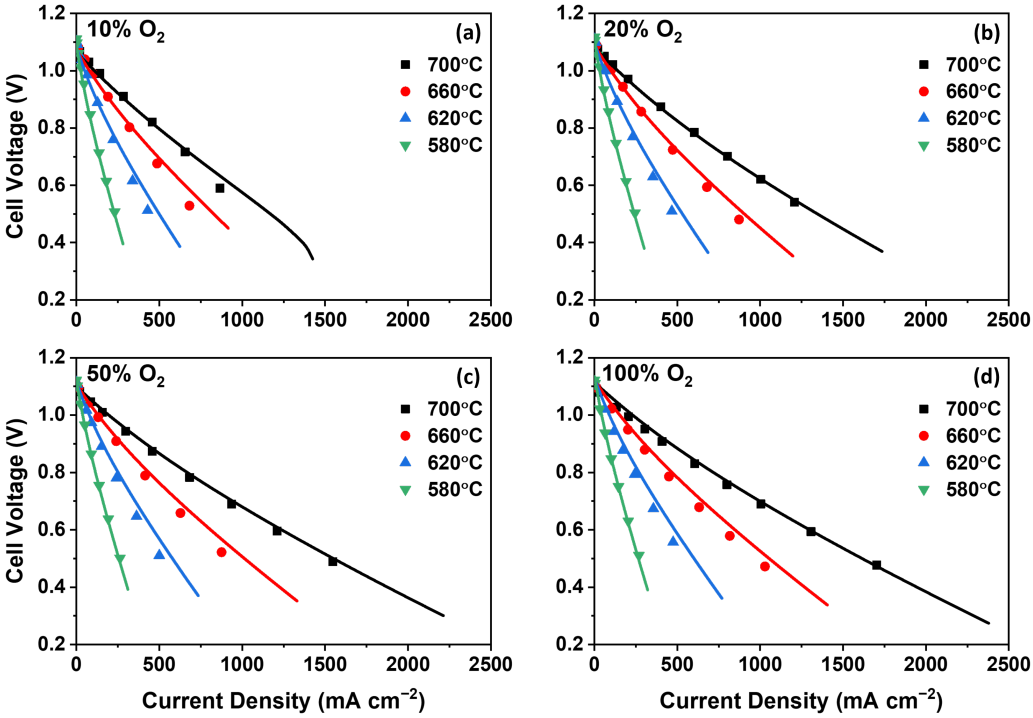

Figure 9. Simulated (lines) and experimental (symbols) polarization curves for 100%, 50%, 30%, and 10% O_2 and 100% H_2 at (**a**) 700 °C, (**b**) 660 °C, (**c**) 620 °C, and (**d**) 580 °C.

Model parameters, including anodic and cathodic gas partial-pressure dependencies (b, m), activation energies ($E_{\mathrm{act,FE}}$, $E_{\mathrm{act,AE}}$), and charge-transfer coefficients (α_{FE}, α_{AE}), were independently extracted through impedance and DRT analyses. The porosity-to-tortuosity factor ψ_{FE} was determined, and the ohmic resistance $\mathrm{ASR}_{\mathrm{ohm}}$ was derived from the high-frequency intercept at OCV and validated via Arrhenius fitting.

Separate methodologies were applied for the determination of structural parameters in the fuel and air electrodes. The porosity-to-tortuosity factor of the fuel electrode, ψ_{FE}, was extracted directly from EIS–DRT analysis by isolating the low-frequency diffusion resistance associated with gas transport through the porous Ni/YSZ substrate. In contrast, a direct experimental extraction of the air-electrode structural parameter, ψ_{AE}, was not feasible under the present operating conditions. As discussed in Section 3.2.6 and demonstrated in the Supplementary Materials, the DRT feature associated with the air electrode represents a lumped polarization process dominated by coupled surface oxygen exchange and bulk oxygen-ion diffusion in the LSCF-based MIEC cathode, rather than pure gas-phase diffusion. The use of pure oxygen and high partial pressures of oxygen further suppresses cathode gas-diffusion limitations, rendering ψ_{AE} non-identifiable from impedance data. To avoid non-physical parameter compensation and overestimation of diffusion-related losses, a literature-based value of $\psi_{\mathrm{AE}} = 0.048$ was therefore adopted for the air electrode. Importantly, this methodological asymmetry does not affect the primary conclusion regarding loss partitioning. Under the investigated operating conditions, the total cell resistance is dominated by ohmic losses, as evidenced by the overpotential decomposition shown in Figure 10a.

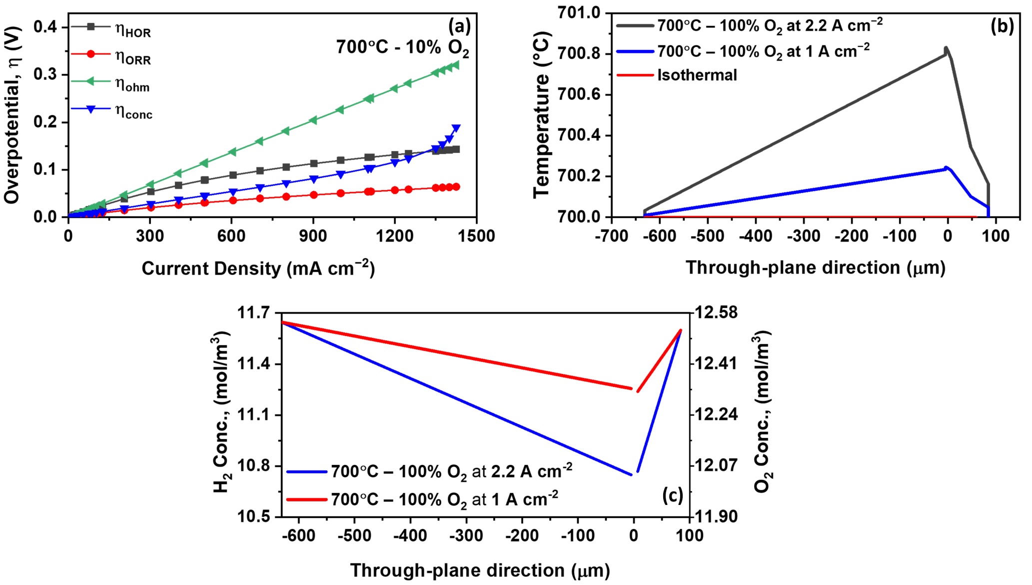

Figure 10. (**a**) The individual overpotential contributions under SOFC operation, namely, the ohmic overpotential η_{ohm}, the activation overpotential η_{act}, and the concentration (gas diffusion) overpotential η_{conc}, are shown as functions of current density j. The operating conditions were 100% H_2 (dry) and 10% O_2 at T = 700 °C. (**b**) Temperature distribution within the cell. (**c**) Concentration distribution within the cell.

Together, these experimentally grounded parameters enabled the model to predict performance with high fidelity, without reliance on empirical curve-fitting. This highlights the model's robustness and the physical relevance of the loss mechanisms across various operating regimes.

5. Discussion and Conclusions

A comprehensive analytical model was developed to predict the electrochemical performance of an anode-supported SOFC. The model demonstrated strong agreement with experimental polarization data across a wide range of operating temperatures (580–700 °C) and oxygen concentrations (10–100% O_2), validating its predictive capability. Activation polarization was modeled using the Butler–Volmer equation, gas diffusion losses were evaluated using Fick's law through extraction of the structural parameters $\psi_{\mathrm{FE}} = 0.198$ and $\psi_{\mathrm{AE}} = 0.048$ (the latter referenced from [45]), and ohmic losses were quantified using Ohm's law, accounting for both electrolyte ionic and interfacial non-ideal contributions.

Key model parameters, including anodic and cathodic Tafel slopes, activation energies, and exchange current densities, were extracted through impedance spectroscopy and DRT analysis performed under OCV conditions. These measurements systematically varied key operating factors, including the fuel composition at the anode, oxidant composition at the cathode, and operating temperature. The resulting impedance spectra were analyzed using an established ECM, enabling the separation of different loss contributions. The extracted resistances were employed to derive the temperature and partial-pressure dependencies of the anodic and cathodic exchange current densities by fitting to semi-empirical power-law expressions. Specifically, the exponents a and b characterize the anodic exchange current density's dependence on the partial pressures of hydrogen and water vapor, while the exponent m captures the cathodic exchange current density's dependence on the partial pressure of oxygen. Charge-transfer coefficients ($\alpha_{\mathrm{FE}} = 0.65$, $\alpha_{\mathrm{AE}} = 0.46$) were determined from fitting activation overpotentials under load.

A significant advancement of this study is the explicit treatment of non-ideal ohmic losses through an effective interfacial resistance term. By analyzing the temperature dependence of the experimentally measured ohmic resistance (ASR_{ohm}) and comparing it with the electrolyte-only contribution predicted from bulk ionic conductivity, a systematic discrepancy was observed, particularly at intermediate and low temperatures. This deviation cannot be attributed solely to electrolyte conduction and instead reflects the cumulative impact of interfacial and contact resistances arising from current-collector interfaces, electrode–electrolyte contact regions, and microstructural non-idealities within the composite electrodes. These effects were captured by extending the ohmic model to include an effective interfacial resistance characterized by an Arrhenius-type temperature dependence, enabling accurate reproduction of the measured ohmic losses across the investigated temperature range.

The second low-frequency peak (P_2) in the impedance spectra of the air electrode does not exclusively reflect gas-phase diffusion resistance through the LSCF–GDC structure but rather a lumped process involving gas diffusion, surface exchange, and charge transfer. As a result, the porosity-to-tortuosity factor (ψ_{AE}) extracted from P_2 is significantly underestimated. This discrepancy further stems from the limited resolution of gas-phase diffusion under the investigated partial pressures of oxygen. As shown in prior analyses of similar cathode structures, gas-phase diffusion can only be distinctly resolved in the DRT spectrum at very low oxygen levels ($P_{\mathrm{O_2,AE}}/P_{\mathrm{ref}} < 0.05$) [39]. To ensure physical accuracy, a literature-based value of $\psi_{\mathrm{AE}} = 0.048$ was adopted, thereby avoiding misattribution of kinetic contributions to mass transport limitations. For the fuel electrode, the structural parameter ψ_{FE} was extracted by varying humidity at the anode side and analyzing the resulting mass transport resistances. To ensure that thermally activated kinetic processes did not interfere with the pure diffusion analysis, ψ_{FE} was calculated only at elevated temperatures (660 °C and 700 °C), where activation losses become negligible compared with diffusion limitations. This extraction methodology, based on linearized forms of the concentration overpotential equations, allowed for a clean extraction of the anode microstructural properties, minimizing artifacts due to kinetic effects.

A non-isothermal formulation was included to assess thermal effects under load; however, the predicted temperature gradients remained below 1 K across the investigated current-density range, confirming quasi-isothermal behavior for the button-cell configuration. Unlike conventional SOFC modeling approaches that rely heavily on empirical curve-fitting, this methodology enables an independent and physically meaningful quantification of each loss mechanism across the full current-density range. This comprehensive analysis facilitates a more precise evaluation of optimization strategies. It enables direct, parameter-based performance comparisons across different regimes based on measurable material and structural properties, offering a robust platform for cell and stack optimization studies. Nevertheless, the current model assumes uniform current density and temperature distributions across the active electrode area, an assumption that is valid primarily for small-area single cells. Deviations from this assumption in larger or segmented cells may lead to inaccuracies in loss prediction and require future extension to more detailed one-, two-, or three-dimensional modeling frameworks.

Future work will focus on expanding the model to capture spatial gradients, degradation phenomena such as electrode delamination or microstructural coarsening, and transient operating conditions. These extensions will further enhance the model's applicability for practical SOFC system design and performance forecasting.

Supplementary Materials: The following supporting information can be downloaded at https://www.mdpi.com/article/10.3390/app16031497/s1, including Figures S1–S4 and Tables S1–S5. Figure S1: Schematic of the SOFC model domain, transport processes, and the equivalent thermal-resistance network with heat sources. Figure S2: Mass balance and temperature distribution calculation algorithm. Figure S3: Determination of charge-transfer coefficients α_{an} and α_{cat}. Panels (a,c,e,g): EIS spectra at $V = \{0.4, 0.6, 0.8, 1.0, \mathrm{OCV}\}$ under 100% O_2 and 100% H_2, and $T = \{700, 660, 620, 580\}$ C. Panels (b,d,f,h): corresponding DRT spectra. Figure S4: Air-electrode lumped resistance from EIS regression: $\mathrm{ASR}_{\mathrm{diff,AE}}$ at 660 and 700 °C, 100%, 50%, 20%, and 10% O_2 and 100% H_2. Table S1: Concentration-dependent pre-exponential factor B_{AE}. Table S2: Pre-exponential factor B_{FE} for different controlled H_2O concentrations. Table S3: Variation of water vapor molar fraction, $X_{\mathrm{H_2O}}$, and γ_{FE} with different controlled H_2O concentrations at various operating temperatures. Table S4: Extracted ohmic resistance values from EIS regression at OCV under different O_2 concentrations. Table S5: Extracted slopes and porosity-to-tortuosity factors ψ_{AE} at different temperatures.

Author Contributions: Conceptualization, J.M.M. and P.-Y.A.C.; methodology, S.S., J.M.M. and H.L.; software, S.S., J.M.M., D.E. and A.W.; validation, J.M.M., D.E., A.W. and P.-Y.A.C.; formal analysis, S.S., J.M.M. and D.E.; investigation, S.S., D.E., J.M.M. and H.L.; resources, M.H.L., A.W. and P.-Y.A.C.; data curation, S.S., J.M.M., H.L. and D.E.; writing—original draft preparation, S.S. and J.M.M.; writing—review and editing, H.L., D.E., A.W., M.H.L. and P.-Y.A.C.; visualization, S.S. and J.M.M.; supervision, M.H.L., A.W. and P.-Y.A.C.; project administration, A.W. and P.-Y.A.C.; funding acquisition, M.H.L., A.W. and P.-Y.A.C. All authors have read and agreed to the published version of the manuscript.

Funding: This research was funded by the University of California, Merced and the SURETECH Program (IIID 2018–009) of the Commission on Higher Education–Philippine California Advanced Research Institutes (CHED–PCARI), Republic of the Philippines.

Data Availability Statement: The data presented in this study are available on request from the corresponding author. The data are not publicly available due to ongoing project restrictions.

Acknowledgments: This work was supported by the University of California, Merced and the SURETECH Program (IID 2018–009) from the Commission on Higher Education, Philippine California Advanced Research Institutes (CHED-PCARI) of the Republic of the Philippines. In addition, Weber and Chuang gratefully acknowledge the Future Mobility Grants funding program within the InnovationCampus Future Mobility (ICM), sponsored by the State of Baden-Württemberg, Germany, for enabling the collaboration between the University of California, Merced and Karlsruhe Institute of Technology.

Conflicts of Interest: The authors declare no conflicts of interest.

Nomenclature

A	Cell-specific constant ($\mathrm{K\,cm^{-1}}$)
$ASR_{O^{2-},ohm}$	Ionic resistance through the electrolyte
$ASR_{contact}$	Contact resistance at interfaces
$ASR_{e^-,ohm}$	Electronic resistance across the electrodes
ASR_{ohm}	Total ohmic resistance
B	Concentration-dependent pre-exponential factor ($\Omega\,\mathrm{cm^2}$)
C_i	Molar concentration of species i ($\mathrm{mol\,cm^{-3}}$)
D_i	Diffusion coefficient of species i ($\mathrm{cm^2\,s^{-1}}$)
E_{act}	Activation energy of the reaction ($\mathrm{kJ\,mol^{-1}}$)
E_{rev}	Thermodynamic reversible voltage (V)
F	Faraday constant ($\mathrm{C\,mol^{-1}}$)
M_i	Molar mass of species i ($\mathrm{kg\,mol^{-1}}$)
N_i''	Molar flux of species i
P	Operating pressure (Pa)
P_{ref}	Reference pressure (1 atm)
R	Universal gas constant (8.314 $\mathrm{J\,mol^{-1}\,K^{-1}}$)
R_{e^-}	Electronic resistance ($\Omega\,\mathrm{cm^2}$)
R_m	Thermal resistance of the electrolyte ($\mathrm{K\,W^{-1}}$)
$R_{th,a}$	Thermal resistance of the anode ($\mathrm{K\,W^{-1}}$)
$R_{th,c}$	Thermal resistance of the cathode ($\mathrm{K\,W^{-1}}$)
T	Operating temperature (K)
T_a	Local temperature at anode–electrolyte interface (K)

T_c	Local temperature at cathode–electrolyte interface (K)
T_m	Local temperature at the center of the electrolyte (K)
T_{ref}	Reference temperature (298 K)
V_{cell}	Cell voltage (V)
a	Exponent: dependency on hydrogen partial pressure
b	Exponent: dependency on water vapor partial pressure
α	Charge-transfer coefficient
δ	Thickness (cm)
$\Delta\hat{C}_p$	Specific heat capacity at constant pressure ($\mathrm{J\,mol^{-1}\,K^{-1}}$)
ΔG	Gibbs free energy of reaction ($\mathrm{kJ\,mol^{-1}}$)
ΔH	Enthalpy of reaction ($\mathrm{kJ\,mol^{-1}}$)
ΔS	Entropy of reaction ($\mathrm{J\,mol^{-1}\,K^{-1}}$)
ϵ	Porosity
η	Overpotential (V)
γ	Pre-exponential factor ($\mathrm{A\,m^{-2}\,K^{-1}}$)
κ	Ionic conductivity at electrode ($\mathrm{S\,cm^{-1}}$)
k_i	Thermal conductivity of solid material i ($\mathrm{W\,m^{-1}\,K^{-1}}$)
ψ	Multiplier for τ/ε in the diffusion medium
ρ	Density ($\mathrm{kg\,m^{-3}}$)
σ	Electrolyte ionic conductivity ($\mathrm{S\,cm^{-1}}$)
τ	Tortuosity factor
x	Partial pressure of a species

References

1. Ghorbani, B.; Vijayaraghavan, K. 3D and simplified pseudo-2D modeling of single cell of a high temperature solid oxide fuel cell to be used for online control strategies. *Int. J. Hydrogen Energy* **2018**, *43*, 9733–9748. [CrossRef]
2. Ishihara, T. *Perovskite Oxide for Solid Oxide Fuel Cells*; Springer: Berlin/Heidelberg, Germany, 2009. [CrossRef]
3. Park, S.; Vohs, J.M.; Gorte, R.J. Direct oxidation of hydrocarbons in a solid-oxide fuel cell. *Nature* **2000**, *404*, 265–267. [CrossRef]
4. Xia, C.; Mi, Y.; Wang, B.; Lin, B.; Chen, G.; Zhu, B. Shaping triple-conducting semiconductor $BaCo_{0.4}Fe_{0.4}Zr_{0.1}Y_{0.1}O_{3-\delta}$ into an electrolyte for low-temperature solid oxide fuel cells. *Nat. Commun.* **2019**, *10*, 1707. [CrossRef]
5. Jeangros, Q.; Bugnet, M.; Epicier, T.; Frantz, C.; Diethelm, S.; Montinaro, D.; Tyukalova, E.; Pivak, Y.; Van Herle, J.; Hessler-Wyser, A.; et al. Operando analysis of a solid oxide fuel cell by environmental transmission electron microscopy. *Nat. Commun.* **2023**, *14*, 7959. [CrossRef]
6. Yao, P.; Yu, H.; Ding, Z.; Liu, Y.; Lu, J.; Lavorgna, M.; Wu, J.; Liu, X. Review on polymer-based composite electrolytes for lithium batteries. *Front. Chem.* **2019**, *7*, 522. [CrossRef]
7. Hussain, S.; Li, Y. Review of solid oxide fuel cell materials: Cathode, anode, and electrolyte. *Energy Transit.* **2020**, *4*, 113–126. [CrossRef]
8. Sun, C.; Stimming, U. Recent anode advances in solid oxide fuel cells. *J. Power Sources* **2007**, *171*, 247–260. [CrossRef]
9. Kaur, G. *Solid Oxide Fuel Cell Components*; Springer: Cham, Switzerland, 2016. Available online: https://link.springer.com/book/10.1007/978-3-319-25598-9 (accessed on 28 January 2026).
10. Subotić, V.; Königshofer, B.; Juričić, Đ.; Kusnezoff, M.; Schröttner, H.; Hochenauer, C.; Boškoski, P. Detailed insight into processes of reversible solid oxide cells and stacks using DRT analysis. *Energy Convers. Manag.* **2020**, *226*, 113509. [CrossRef]
11. Yue, W.; Li, Y.; Zheng, Y.; Wu, T.; Zhao, C.; Zhao, J.; Geng, G.; Zhang, W.; Chen, J.; Zhu, J.; et al. Enhancing coking resistance of Ni/YSZ electrodes: In situ characterization, mechanism research, and surface engineering. *Nano Energy* **2019**, *62*, 64–78. [CrossRef]
12. Marcantonio, V.; Del Zotto, L.; Ouweltjes, J.P.; Bocci, E. Main issues of the impact of tar, H_2S, HCl and alkali metal from biomass-gasification derived syngas on the SOFC anode and the related gas cleaning technologies for feeding a SOFC system: A review. *Int. J. Hydrogen Energy* **2022**, *47*, 517–539. [CrossRef]
13. Chen, Y.; Yoo, S.; Li, X.; Ding, D.; Pei, K.; Chen, D.; Ding, Y.; Zhao, B.; Murphy, R.; deGlee, B.; et al. An effective strategy to enhancing tolerance to contaminants poisoning of solid oxide fuel cell cathodes. *Nano Energy* **2018**, *47*, 474–480. [CrossRef]
14. Mogensen, M.B.; Chen, M.; Frandsen, H.L.; Graves, C.; Hauch, A.; Hendriksen, P.V.; Jacobsen, T.; Jensen, S.H.; Skafte, T.L.; Sun, X. Ni migration in solid oxide cell electrodes: Review and revised hypothesis. *Fuel Cells* **2021**, *21*, 415–429. [CrossRef]
15. Tao, J.; Yao, G.; Komatsu, Y.; Sciazko, A.; Lyu, Z.; Okabe, T.; Nishimura, K.; Shikazono, N. Effect of anodic polarization on morphology changes of Ni-YSZ patterned fuel electrode of solid oxide fuel cell. *Acta Mater.* **2026**, *305*, 121867. [CrossRef]
16. Yao, G.; Okabe, T.; Shikazono, N. Ni migration on porous yttria-stabilized zirconia and yttria-micropatterned fuel electrodes in solid oxide fuel cells. *J. Power Sources* **2024**, *609*, 234720. [CrossRef]

17. Zhang, Y.; Chen, B.; Guan, D.; Xu, M.; Ran, R.; Ni, M.; Zhou, W.; O'Hayre, R.; Shao, Z. Thermal-expansion offset for high-performance fuel cell cathodes. *Nature* **2021**, *591*, 246–251. [CrossRef] [PubMed]
18. Duan, Y.; Li, H.; Li, S.; Zhou, Y.; Liu, R.; Gao, Z.; Guan, W.; Yang, J.; Wang, J.; Wan, X.; et al. Thermal Expansion Matching as a Key Criterion for Developing High-Performance Mn-based Mullite Cathodes in SOFCs. *Adv. Mater.* **2026**, *38*, e13615. [CrossRef] [PubMed]
19. Blum, L. An Analysis of Contact Problems in Solid Oxide Fuel Cell Stacks Arising from Differences in Thermal Expansion Coefficients. *Electrochim. Acta* **2017**, *223*, 100–108. [CrossRef]
20. Zheng, H.; Jiang, W.; Luo, Y.; Song, M.; Zhang, X.; Tu, S.T. Coupled degradation mechanism of electrochemical and mechanical performance of solid oxide fuel cells under thermal cycling. *Appl. Energy* **2025**, *381*, 125187. [CrossRef]
21. Han, X.; Ling, Y.; Yang, Y.; Wu, Y.; Gao, Y.; Wei, B.; Lv, Z. Utilizing High Entropy Effects for Developing Chromium-Tolerance Cobalt-Free Cathode for Solid Oxide Fuel Cells. *Adv. Funct. Mater.* **2023**, *33*, 2304728. [CrossRef]
22. Minh, N.Q. Ceramic Fuel Cells. *J. Am. Ceram. Soc.* **1993**, *76*, 563–588. [CrossRef]
23. Fakhimi Bonab, M.; Elcombe, G.; Garcia, T.; Lee, M.H. Binary Dopant Exsolution in La–Sr–Ti Perovskites Via Near-Ambient-Pressure XPS. In Proceedings of the ECS Meeting Abstracts. The Electrochemical Society, Chicago, IL, USA, 12–16 October 2025; Volume MA2025-02, p. 2271. [CrossRef]
24. Primdahl, S.; Mogensen, M. Gas Diffusion Impedance in Characterization of Solid Oxide Fuel Cell Anodes. *J. Electrochem. Soc.* **1999**, *146*, 2827–2833. [CrossRef]
25. Kakaç, S.; Pramuanjaroenkij, A.; Zhou, X.Y. A review of numerical modeling of solid oxide fuel cells. *Int. J. Hydrogen Energy* **2007**, *32*, 761–786. [CrossRef]
26. Wang, K.; Hissel, D.; Péra, M.C.; Steiner, N.; Marra, D.; Sorrentino, M.; Pianese, C.; Monteverde, M.; Cardone, P.; Saarinen, J. A review on solid oxide fuel cell models. *Int. J. Hydrogen Energy* **2011**, *36*, 7212–7228. [CrossRef]
27. Wang, G.; Yang, Y.; Zhang, H.; Xia, W. 3-D model of thermo-fluid and electrochemical for planar SOFC. *J. Power Sources* **2007**, *167*, 398–405. [CrossRef]
28. Yakabe, H.; Sakurai, T. 3D simulation on the current path in planar SOFCs. *Solid State Ionics* **2004**, *174*, 295–302. [CrossRef]
29. Gubner, A. Non-Isothermal and Dynamic SOFC Voltage-Current Behavior. In *Proceedings of the ECS Proceedings Volumes: Ninth International Symposium on Solid Oxide Fuel Cells (SOFC-IX), Québec City, QC, Canada, 15–20 May 2005*; The Electrochemical Society: Pennington, NJ, USA, 2005; Volume 2005-07, p. 814. [CrossRef]
30. Gubner, A.; Froning, D.; de Haart, B.; Stolten, D. Complete Modeling of kW-Range SOFC Stacks. In *Proceedings of the ECS Proceedings Volumes: Eighth International Symposium on Solid Oxide Fuel Cells (SOFC-VIII), Paris, France, 27 April–2 May 2003*; The Electrochemical Society: Pennington, NJ, USA, 2003; Volume 2003-07, p. 1436. [CrossRef]
31. Aloui, T.; Halouani, K. Analytical modeling of polarizations in a solid oxide fuel cell using biomass syngas product as fuel. *Appl. Therm. Eng.* **2007**, *27*, 731–737. [CrossRef]
32. Bao, C.; Zhang, X. One-dimensional macroscopic model of solid oxide fuel cell anode with analytical modeling of H_2/CO electrochemical co-oxidation. *Electrochim. Acta* **2014**, *134*, 426–434. [CrossRef]
33. Zhao, F.; Virkar, A.V. Dependence of polarization in anode-supported solid oxide fuel cells on various cell parameters. *J. Power Sources* **2005**, *141*, 79–95. [CrossRef]
34. Hussain, M.M.; Li, X.; Dincer, I. Mathematical modeling of planar solid oxide fuel cells. *J. Power Sources* **2006**, *161*, 1012–1022. [CrossRef]
35. Costamagna, P.; Costa, P.; Antonucci, V. Micro-modelling of solid oxide fuel cell electrodes. *Electrochim. Acta* **1998**, *43*, 375–394. [CrossRef]
36. Chan, S.H.; Xia, Z.T. Anode Micro Model of Solid Oxide Fuel Cell. *J. Electrochem. Soc.* **2001**, *148*, A388–A394. [CrossRef]
37. Pramuanjaroenkij, A.; Kakaç, S.; Zhou, X.Y. Mathematical analysis of planar solid oxide fuel cells. *Int. J. Hydrogen Energy* **2008**, *33*, 2547–2565. [CrossRef]
38. Grimes, J.; Hong, J.; Barnett, S.A. Effect of Gd-doped ceria infiltration into Ni–YSZ on reversible solid oxide cell operation. *J. Power Sources* **2022**, *551*, 232189. [CrossRef]
39. Leonide, A.; Apel, Y.; Ivers-Tiffée, E. SOFC modeling and parameter identification by means of impedance spectroscopy. *ECS Trans.* **2009**, *19*, 81–92. [CrossRef]
40. Ivers-Tiffée, E.; Weber, A. Evaluation of electrochemical impedance spectra by the distribution of relaxation times. *J. Ceram. Soc. Jpn.* **2017**, *125*, 193–201. [CrossRef]
41. Riegraf, M.; Costa, R.; Schiller, G.; Friedrich, K.A.; Dierickx, S.; Weber, A. Electrochemical Impedance Analysis of Symmetrical Ni/Gadolinium-Doped Ceria (CGO10) Electrodes in Electrolyte-Supported Solid Oxide Cells. *J. Electrochem. Soc.* **2019**, *166*, F865–F876. [CrossRef]
42. Hong, J.; Bhardwaj, A.; Bae, H.; Kim, I.h.; Song, S.J. Electrochemical Impedance Analysis of SOFC with Transmission Line Model Using Distribution of Relaxation Times (DRT). *J. Electrochem. Soc.* **2020**, *167*, 114504. [CrossRef]
43. Leonide, A. Modeling of Solid Oxide Fuel Cell Electrodes Using Impedance Spectroscopy. Ph.D. Thesis, Karlsruhe Institute of Technology, Karlsruhe, Germany, 2009.

44. Geisler, H.I. Finite Element Method (FEM) Model and Performance Analysis of Solid Oxide Fuel Cells. Ph.D. Thesis, Karlsruhe Institute of Technology (KIT), Karlsruhe, Germany, 2014. [CrossRef]
45. Grosselindemann, C.; Russner, N.; Dierickx, S.; Wankmüller, F.; Weber, A. Deconvolution of gas diffusion polarization in Ni/gadolinium-doped ceria fuel electrodes. *J. Electrochem. Soc.* **2021**, *168*, 124506. [CrossRef]
46. Mueller, M.; Klinsmann, M.; Sauter, U.; Njodzefon, J.C.; Weber, A. Parametrization of a 0D solid oxide cell performance model—A detailed investigation including temperature dependencies of kinetic parameters. *J. Physics: Energy* **2025**, *7*, 045006. [CrossRef]
47. Matsuda, J.; Kanae, S.; Kawabata, T.; Chou, J.T.; Inoue, Y.; Taniguchi, S.; Sasaki, K. TEM and ETEM Study on $SrZrO_3$ Formation at the LSCF/GDC/YSZ Interfaces. *ECS Trans.* **2017**, *78*, 993–1000. [CrossRef]
48. Lu, Z.; Darvish, S.; Hardy, J.; Templeton, J.; Stevenson, J.; Zhong, Y. $SrZrO_3$ formation at the interlayer/electrolyte interface during $(La_{1-x}Sr_x)_{1-\delta}Co_{1-y}Fe_yO_3$ cathode sintering. *J. Electrochem. Soc.* **2017**, *164*, F3097–F3103. [CrossRef]
49. Develos-Bagarinao, K.; Ishiyama, T.; Kishimoto, H.; Shimada, H.; Yamaji, K. Nanoengineering of cathode layers for solid oxide fuel cells to achieve superior power densities. *Nat. Commun.* **2021**, *12*, 3979. [CrossRef]
50. Li, H.; Kim, H.J.; Garcia, T.J.; Park, G.; Ding, Y.; Liu, M.; An, J.; Lee, M.H. Ultralow Loading of Ru as a Bifunctional Catalyst for the Oxygen Electrode of Solid Oxide Cells. *ACS Catal.* **2023**, *13*, 11172–11181. [CrossRef] [PubMed]
51. Wan, T.H.; Saccoccio, M.; Chen, C.; Ciucci, F. Influence of the discretization methods on the distribution of relaxation times deconvolution: Implementing radial basis functions with DRTtools. *Electrochim. Acta* **2015**, *184*, 483–499. [CrossRef]
52. Maric, R. *Solid Oxide Fuel Cells: From Fundamental Principles to Complete Systems*; CRC Press: Boca Raton, FL, USA, 2020. [CrossRef]
53. Weng, F.B.; Dlamini, M.M.; Jung, G.B.; Lian, C.X. Analyses of reversible solid oxide cells porosity effects on temperature reduction. *Int. J. Hydrogen Energy* **2020**, *45*, 12170–12184. [CrossRef]
54. O'Hayre, R.; Cha, S.W.; Colella, W.; Prinz, F.B. *Fuel Cell Fundamentals*, 3rd ed.; John Wiley & Sons: Hoboken, NJ, USA, 2016. [CrossRef]
55. Akhtar, N.; Decent, S.P.; Loghin, D.; Kendall, K. A three-dimensional numerical model of a single-chamber solid oxide fuel cell. *Int. J. Hydrogen Energy* **2009**, *34*, 8645–8663. [CrossRef]
56. Andersson, M.; Yuan, J.; Sundén, B. Review on modeling development for multiscale chemical reactions coupled transport phenomena in solid oxide fuel cells. *Appl. Energy* **2010**, *87*, 1461–1476. [CrossRef]
57. Wendt, H.; Kreysa, G. *Electrochemical Engineering: Science and Technology in Chemical and Other Industries*, 1st ed.; Springer: Berlin, Heidelberg, 1999. [CrossRef]
58. Xing, Y.; Costa-Castelló, R.; Na, J.; Renaudineau, H. Control-oriented modelling and analysis of a solid oxide fuel cell system. *Int. J. Hydrogen Energy* **2020**, *45*, 20659–20672. [CrossRef]
59. Naterer, G.F.; Tokarz, C.D.; Avsec, J. Fuel cell entropy production with ohmic heating and diffusive polarization. *Int. J. Heat Mass Transf.* **2006**, *49*, 2673–2683. [CrossRef]
60. Shen, S.; Yang, Y.; Guo, L.; Liu, H. A polarization model for a solid oxide fuel cell with a mixed ionic and electronic conductor as electrolyte. *J. Power Sources* **2014**, *256*, 43–51. [CrossRef]
61. Ewald, D.; Grosselindemann, C.; Esau, D.; Fuchs, F.M.; Weber, A. Stack-like contacting in solid oxide cells: Electrochemical characterization and modeling. *J. Electrochem. Soc.* **2024**, *171*, 044506. [CrossRef]
62. Tian, Y.; Zhang, H.; Li, G.; Hu, Y.; Fan, L.; Jia, L. Optimizing cathode contact layer thickness for enhanced efficiency and durability in solid oxide fuel cell stacks. *Mater. Sci. Eng. B* **2026**, *323*, 118827. [CrossRef]
63. Slomski, H.S.; Rowberg, A.J.E.; Van Winkle, M.; Nagle-Cocco, L.A.V.; Strange, N.A.; Kane, N.; Hartvigsen, J.L.; Casteel, M.J.; Ginley, D.S.; Wood, B.C.; et al. The structure, composition, and performance impact of a YSZ–GDC interdiffusion layer in solid oxide electrolysis cells. *J. Power Sources* **2026**, *669*, 239398. [CrossRef]
64. Mendoza, R.M.O.; Mora, J.M.; Cervera, R.B.; Chuang, P.Y.A. Experimental and Analytical Study of an Anode-Supported Solid Oxide Electrolysis Cell. *Chem. Eng. Technol.* **2020**, *43*, 2350–2358. [CrossRef]
65. Lin, Y.; Beale, S.B. Performance predictions in solid oxide fuel cells. *Appl. Math. Model.* **2006**, *30*, 1485–1496. [CrossRef]
66. Yuan, J.; Huang, Y.; Sundén, B.; Wang, W.G. Analysis of parameter effects on chemical reaction coupled transport phenomena in SOFC anodes. *Heat Mass Transf.* **2009**, *45*, 471–484. [CrossRef]
67. Dillig, M.; Biedermann, T.; Karl, J. Thermal contact resistance in solid oxide fuel cell stacks. *J. Power Sources* **2015**, *300*, 69–76. [CrossRef]
68. Gavrilyuk, A.L.; Osinkin, D.A.; Bronin, D.I. The use of Tikhonov regularization method for calculating the distribution function of relaxation times in impedance spectroscopy. *Russ. J. Electrochem.* **2017**, *53*, 575–588. [CrossRef]
69. Xia, J.; Wang, C.; Wang, X.; Bi, L.; Zhang, Y. A perspective on DRT applications for the analysis of solid oxide cell electrodes. *Electrochim. Acta* **2020**, *355*, 136328. [CrossRef]
70. Leonide, A.; Sonn, V.; Weber, A.; Ivers-Tiffée, E. Evaluation and Modeling of the Cell Resistance in Anode-Supported Solid Oxide Fuel Cells. *J. Electrochem. Soc.* **2008**, *155*, B36–B41. [CrossRef]
71. Adler, S.B. Factors Governing Oxygen Reduction in Solid Oxide Fuel Cell Cathodes. *Chem. Rev.* **2004**, *104*, 4791–4844. [CrossRef]
72. Evans, A.; Bieberle-Hütter, A.; Rupp, J.L.M.; Gauckler, L.J. Review on microfabricated micro-solid oxide fuel cell membranes. *J. Power Sources* **2009**, *194*, 119–129. [CrossRef]

73. Klotz, D.; Weber, A.; Ivers-Tiffée, E. Practical Guidelines for Reliable Electrochemical Characterization of Solid Oxide Fuel Cells. *Electrochim. Acta* **2017**, *227*, 110–126. [CrossRef]
74. Jiang, S.P. A comparison of O_2 reduction reactions on porous (La,Sr)MnO_3 and (La,Sr)(Co,Fe)O_3 electrodes. *Solid State Ionics* **2002**, *146*, 1–22. [CrossRef]
75. Brant, M.C.; Matencio, T.; Dessemond, L.; Domingues, R.Z. Electrical degradation of porous and dense LSM/YSZ interface. *Solid State Ionics* **2006**, *177*, 915–921. [CrossRef]
76. Benamira, M.; Ringuedé, A.; Cassir, M.; Horwat, D.; Pierson, J.F.; Lenormand, P.; Ansart, F.; Bassat, J.M.; Fullenwarth, J. Comparison between ultrathin films of YSZ deposited at the solid oxide fuel cell cathode/electrolyte interface by atomic layer deposition, dip-coating or sputtering. *Open Fuels Energy Sci. J.* **2009**, *2*, 87–99. [CrossRef]
77. Yang, J.; Muroyama, H.; Matsui, T.; Eguchi, K. A comparative study on polarization behavior of (La, Sr)MnO_3 and (La, Sr)CoO_3 cathodes for solid oxide fuel cells. *Int. J. Hydrogen Energy* **2010**, *35*, 10505–10512. [CrossRef]
78. Hjalmarsson, P.; Mogensen, M. $La_{0.99}Co_{0.4}Ni_{0.6}O_{3-\delta}$–$Ce_{0.8}Gd_{0.2}O_{1.95}$ as composite cathode for solid oxide fuel cells. *J. Power Sources* **2011**, *196*, 7237–7244. [CrossRef]
79. Im, J.; Park, I.; Shin, D. Preparation of nano-crystalline strontium-doped lanthanum manganate (LSM) powder and porous film by aerosol flame deposition. *Ceram. Int.* **2014**, *40*, 5567–5573. [CrossRef]
80. Seyed-Vakili, S.V.; Babaei, A.; Ataie, M.; Heshmati-Manesh, S.; Abdizadeh, H. Enhanced performance of $La_{0.8}Sr_{0.2}MnO_3$ cathode for solid oxide fuel cells by co-infiltration of metal and ceramic precursors. *J. Alloy. Compd.* **2018**, *737*, 433–441. [CrossRef]
81. Holtappels, P.; Vinke, I.C.; de Haart, L.G.J.; Stimming, U. Reaction of hydrogen/water mixtures on nickel-zirconia cermet electrodes: II. AC polarization characteristics. *J. Electrochem. Soc.* **1999**, *146*, 2976–2982. [CrossRef]
82. Jiang, S.P.; Badwal, S.P.S. An electrode kinetics study of H_2 oxidation on Ni/Y_2O_3–ZrO_2 cermet electrode of the solid oxide fuel cell. *Solid State Ionics* **1999**, *123*, 209–224. [CrossRef]
83. Karmhag, R.; Niklasson, G.A.; Nygren, M. Oxidation kinetics of nickel nanoparticles. *J. Appl. Phys.* **2001**, *89*, 3012–3017. [CrossRef]
84. Suwanwatana, W.; Yarlagadda, S.; Gillespie, J.W. An investigation of oxidation effects on hysteresis heating of nickel particles. *J. Mater. Sci.* **2003**, *38*, 565–573. [CrossRef]
85. Haugsrud, R. On the high-temperature oxidation of nickel. *Corros. Sci.* **2003**, *45*, 211–235. [CrossRef]
86. Waldbillig, D.; Wood, A.; Ivey, D.G. Thermal analysis of the cyclic reduction and oxidation behaviour of SOFC anodes. *Solid State Ionics* **2005**, *176*, 847–859. [CrossRef]
87. Richardson, J.T.; Scates, R.; Twigg, M.V. X-ray diffraction study of nickel oxide reduction by hydrogen. *Appl. Catal. A Gen.* **2003**, *246*, 137–150. [CrossRef]
88. Osinkin, D.A.; Bogdanovich, N.M.; Beresnev, S.M.; Zhuravlev, V.D. High-performance anode-supported solid oxide fuel cell with impregnated electrodes. *J. Power Sources* **2015**, *288*, 20–25. [CrossRef]
89. Doppler, M.C.; Fleig, J.; Bram, M.; Opitz, A.K. Hydrogen oxidation mechanisms on Ni/yttria stabilized zirconia anodes: Separation of reaction pathways by geometry variation of pattern electrodes. *J. Power Sources* **2018**, *380*, 46–54. [CrossRef]
90. Luo, Y.; Li, W.; Shi, Y.; Wang, Y.; Cai, N. Reversible H_2/H_2O electrochemical conversion mechanisms on the patterned nickel electrodes. *Int. J. Hydrogen Energy* **2017**, *42*, 25130–25142. [CrossRef]
91. Petruzzi, L.; Cocchi, S.; Fineschi, F. A global thermo-electrochemical model for SOFC systems design and engineering. *J. Power Sources* **2003**, *118*, 96–107. [CrossRef]
92. Aguiar, P.; Adjiman, C.S.; Brandon, N.P. Anode-supported intermediate temperature direct internal reforming solid oxide fuel cell. I: Model-based steady-state performance. *J. Power Sources* **2004**, *138*, 120–136. [CrossRef]
93. Weber, A. Testing of Solid Oxide Cells at High Current Densities. *Tm-Tech. Mess.* **2022**, *89*, 97–106. [CrossRef]
94. Sonn, V.; Leonide, A.; Ivers-Tiffée, E. Combined Deconvolution and CNLS Fitting Approach Applied on the Impedance Response of Technical Ni/8YSZ Cermet Electrodes. *J. Electrochem. Soc.* **2008**, *155*, B675–B679. [CrossRef]
95. Butz, B.; Lefarth, A.; Störmer, H.; Utz, A.; Ivers-Tiffée, E.; Gerthsen, D. Accelerated degradation of 8.5 mol% Y_2O_3-doped zirconia by dissolved Ni. *Solid State Ionics* **2012**, *214*, 37–44. [CrossRef]
96. Tsoga, A.; Gupta, A.; Naoumidis, A.; Nikolopoulos, P. Gadolinia-doped ceria and yttria-stabilized zirconia interfaces: regarding their application for SOFC technology. *Acta Mater.* **2000**, *48*, 4709–4714. [CrossRef]
97. Szász, J.; Wankmüller, F.; Wilde, V.; Störmer, H.; Gerthsen, D.; Menzler, N.H.; Ivers-Tiffée, E. Nature and Functionality of $(La_{0.58}Sr_{0.4})Co_{0.2}Fe_{0.8}O_{3-\delta}$ / $Gd_{0.2}Ce_{0.8}O_{2-\delta}$ / $Y_{0.16}Zr_{0.84}O_{2-\delta}$ Interfaces in SOFCs. *J. Electrochem. Soc.* **2018**, *165*, F898–F906. [CrossRef]
98. Golani, S.; Wankmüller, F.; Herzhof, W.; Dellen, C.; Menzler, N.H.; Weber, A. Impact of GDC Interlayer Microstructure on Strontium Zirconate Interphase Formation and Cell Performance. *J. Electrochem. Soc.* **2023**, *170*, 104501. [CrossRef]
99. Rowberg, A.J.E.; Slomski, H.S.; Kim, N.; Strange, N.A.; Gorman, B.P.; Shulda, S.; Ginley, D.S.; Kweon, K.E.; Wood, B.C. Impact of Sr-Containing Secondary Phases on Oxide Conductivity in Solid-Oxide Electrolyzer Cells. *Chem. Mater.* **2024**, *36*, 6464–6474. [CrossRef]
100. Ju, H.; Wang, C.Y. Experimental Validation of a PEM Fuel Cell Model by Current Distribution Data. *J. Electrochem. Soc.* **2004**, *151*, A1954–A1960. [CrossRef]

101. Mora, J.M.; Sarker, M.; Najafianashrafi, Z.; Rahman, M.A.; Yang-Neyerlin, A.C.; Pivovar, B.; Chuang, P.Y.A. Analytical-based Simulation Approach for an Anion Exchange Membrane Fuel Cell. *J. Power Sources* **2021**, *510*, 230443. [CrossRef]
102. Rizvandi, O.B.; Jensen, S.H.; Frandsen, H.L. A modeling study of lifetime and performance improvements of solid oxide fuel cell by reversed pulse operation. *J. Power Sources* **2022**, *523*, 231048. [CrossRef]
103. Weber, A. Impedance analysis of porous electrode structures in batteries and fuel cells. *Tm-Tech. Mess.* **2021**, *88*, 1–16. [CrossRef]
104. Kong, W.; Li, J.; Liu, S.; Lin, Z. The influence of interconnect ribs on the performance of planar solid oxide fuel cell and formulae for optimal rib sizes. *J. Power Sources* **2012**, *204*, 106–115. [CrossRef]
105. Liu, S.; Song, C.; Lin, Z. The effects of the interconnect rib contact resistance on the performance of planar solid oxide fuel cell stack and the rib design optimization. *J. Power Sources* **2008**, *183*, 214–225. [CrossRef]